Inviscid evolution of stretched vortex arrays

By D. I. PULLIN AND P. A. JACOBS

Department of Mechanical Engineering, University of Queensland, St Lucia, 4067, Australia

The nonlinear evolution of an array of pairs of inviscid counter-rotating vortices, subjected to an applied stretching strain field, has been studied numerically using the contour-dynamics method. The array configuration is effectively the Corcos–Lin model of streamwise vortices in the braid region of a nominally two-dimensional mixing layer. For each individual vortex the simulations elucidate the strong interaction between the vortex self-induction, the vorticity amplification of the stretching strain, and the local in-plane strain applied by all other members of the array. When the initial vorticity distribution is modelled by a non-uniform piece-wise-constant vorticity field defined over a nested set of non-intersecting contours, the dynamical evolution reveals fine structure consisting of strong vortex roll-up accompanied by trailing, filament-like spiral vortex sheets, and the presence of tertiary instabilities. It is shown by a particular example that these features are largely absent in an equivalent computation in which array members are modelled by the commonly used uniform-vortex approximation.

1. Introduction

There is now substantial experimental evidence which indicates the existence of a system of longitudinal streamwise vortices located within the thin shear-layer regions (the braids) connecting the spanwise vortex cores of the nominally two-dimensional mixing layer. Using the visual product of a chemical reaction as a flow-visualization technique, Breidenthal (1981) observed organized streamwise structures in a mixing layer with average spanwise wavelength scaled on the initial wavelength of the two-dimensional primary shear-layer instability. Bernal (1981) obtained pictures through planes normal to the stream in the braid region that show what appear to be cross-sections of spiral streamwise vortices. Hot-wire measurements in the mixing layer (Jimenez 1983) together with digital image processing of flow-visualization photographs (Jimenez, Cogollas & Bernal 1985) support the spanwise scaling found by Breidenthal and further indicate that the mean circulation of individual streamwise structures increases to a nearly constant value of the same order as the local circulation in the primary, rolled-up spanwise vortices.

Roshko (1980) suggested that a set of spanwise and streamwise vortices would naturally play an important dynamical role in the transition of the mixing layer to three-dimensionality, and that for Reynolds numbers tending to infinity, further groups of higher-order structures would be required to accomplish energy transfer to the finer scales of motion. A convincing deterministic paradigm of this process has been described by Corcos & Sherman (1984), Corcos & Lin (1984) and Lin & Corcos (1984), motivated by the idea that at least the initial phase of transition in the mixing layer is not wholly chaotic but occurs in a more or less ordered hierarchy of characteristic vortex structures which interact via a system of identifiable, nonlinear

instabilities. The second level of the Corcos–Lin–Sherman (CLS) model consists of an array of highly flattened, nearly streamwise counter-rotating vortices embedded within the vorticity-depleted primary braid system, and subject to the local stretching-strain field produced by the spanwise rolled-up vortex cores (Lin & Corcos 1984). Although the process whereby streamwise vorticity of zero spanwise average value might be produced from the original spanwise shear layer is not yet fully understood, these secondary vortices of the CLS model are natural prototypes for the streamwise structures seen in experiments. They therefore seem worthy of further study.

In the present paper we apply the inviscid contour-dynamics (CD) method (Zabusky, Hughes & Roberts 1979) to simulate the Corcos–Lin model of secondary vortex evolution. In §2 we describe briefly the CLS hierarchy of deterministic motions in the mixing layer. The CD model is formulated in §3. Each vortex is modelled by a piecewise-constant vorticity distribution defined over four layers of uniform-vorticity fluid, introduced to model vorticity gradients that are shown to be significant for the flow development. The numerical method is described briefly in §4 and in Appendix B, and the initial conditions and flow parameters are given in §5. The simulations which are discussed in §6 reveal the formation of intense cores at the centre of each rotating vortex, together with spiral vortex sheets and the appearance of local instabilities on the strained outer vortex layer.

2. The Corcos–Lin model of secondary vortices in a mixing layer

The Corcos–Lin–Sherman model of the mixing layer is depicted in figure 1. The version shown is a standard idealized approximation of a laboratory-generated shear layer. The latter develops in the streamwise direction and at a fixed streamwise station its fluid properties are nearly periodic in time. In contrast the model layer is periodic in the streamwise direction but evolves in time. In figure 1 the primary or first-order motion is the nominally two-dimensional instability of the parallel shear flow. If δ_1 is the initial layer vorticity thickness, and U the velocity shear, the primary (Kelvin–Helmholtz) instability has maximum growth rate on a streamwise lengthscale $L \approx 7.5\,\delta_1$ leading to vortex roll-up into compact primary spanwise cores of circulation $\Gamma \approx UL$, and on a timescale $T_1 = O(L/U)$. Subsequent subharmonic pairing instabilities follow giving the well-known streamwise linear growth in the mean layer thickness.

The second-order motion is the growth of three-dimensional perturbations on the time-dependent base flow of the primary vortices. There are several plausible mechanisms that might generate strong streamwise vorticity from such instabilities. It is clear however that the classical linearized Orr–Sommerfeld instability of the parallel shear layer is not appropriate since the predicted timescale for the growth of three-dimensional motions is larger than that required for the appearance of strongly nonlinear features such as roll-up and pairing, which ultimately emerge from a purely two-dimensional instability. This led Pierrehumbert & Widnall (1982) to study the inviscid modulational three-dimensional instability of Stuart vortices, used as a model of the rolled-up state of the primary vortex structures. They found new three-dimensional wavelike growing modes – the 'translative' instability – centred within the concentrated vortex cores, over a broad range of spanwise wavelengths which included the streamwise wavelength of the Stuart vortices. Corcos & Lin (1984) argue however that the translative instability is both slower than, and is inhibited by, the pairing instability of the primary vortices, and that consequently the
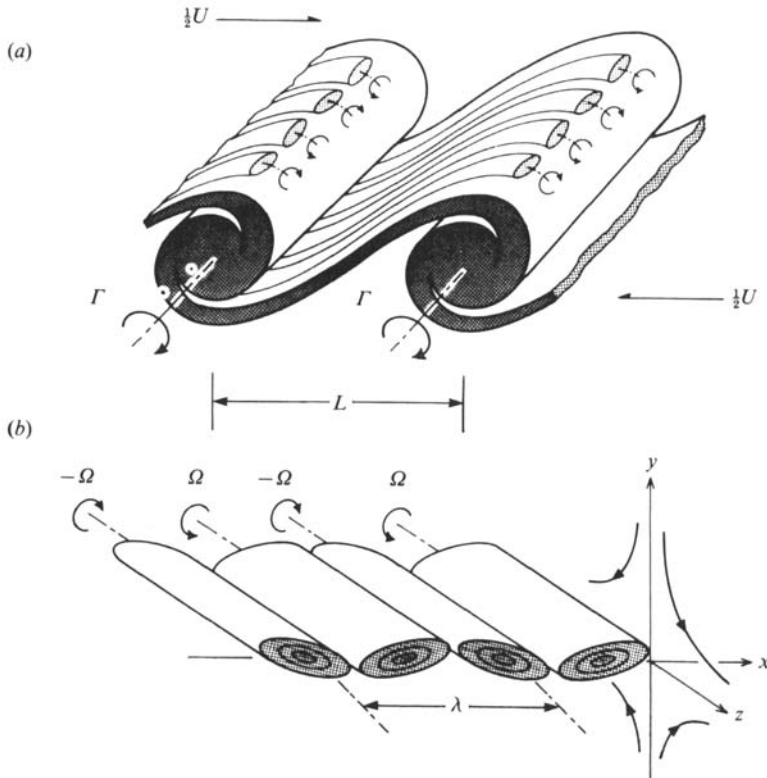
FIGURE 1. (a) Primary rolled-up vortices in a free shear layer and secondary vortices (not to scale spanwise) in the braid region. (b) Corcos–Lin model of secondary vortices subject to locally uniform three-dimensional strain induced by the primary vortices.

assumption of a steady albeit non-uniform base flow implicit in the use of Stuart vortices is not appropriate to the shear-layer evolution. They studied the origin of the three-dimensional motion at a shear-layer Reynolds number $Re_1 = U\delta_1/\nu = 50$ (ν is the kinematic viscosity) as an initial-value problem obtained through linearization of the three-dimensional velocity about the spanwise average of the total velocity field. All perturbation properties were assumed to have periodic spanwise variation. Non-spanwise vorticity was found to grow from the initial three-dimensional disturbances in both the primary vortex cores and in the braid regions. In the former it tended to be folded several times and to rotate with the cores, while in the latter it remained sensibly tangent to the braid in the plane of the unperturbed shear flow. Significantly Corcos & Lin found that three-dimensional motions, even at large amplitudes, had negligible influence on the two-dimensional base flow. They conclude that the origin of the experimentally observed streamwise vorticity lies essentially within the braids, resulting from a three-dimensional Orr–Sommerfeld-type instability of the initial shear layer modified substantially by the nonlinear time history of the two-dimensional base flow, at least up to the first pairing event.

Whatever the origins of the three-dimensional motions, it is apparent that their effect is the creation of an array of streamwise counter-rotating secondary vortices (figure 1 b), whose axes are locally tangent to the braids. The calculations discussed previously do not give information on either their average spanwise wavelength λ or on the individual vortex circulation Ω but experimental evidence suggests $\lambda \approx L$

(Breidenthal 1981) and $\Omega = \beta \Gamma$ where $\beta = O(1)$ (Jimenez 1983). According to the CLS model the secondary vortices lie within the axial stretching strain with magnitude $\gamma = \pi U/(2L)$ (this value is obtained from a point-vortex model) induced in the braid region by the primary vortices (Corcos & Lin 1984). The strain compresses the vortices normal to the local tangent plane containing the braids so that, within a linearized approximation, their vorticity thickness δ_ω approaches the Burgers vortex-sheet thickness $\delta_2 = (2\pi \nu/\gamma)^{\frac{1}{2}}$ (Burgers 1948) in a time of order $T_2 \approx \gamma^{-1}[\delta_1^2/\delta_2^2 - 1]^{\frac{1}{2}}$ (Lin & Corcos 1984; hereinafter referred to as LC). Cross-sections of the vortex cores then tend towards a flattened shape elongated in the spanwise direction. In our notation T_2 and the asymptotic aspect ratio $a_1 = \lambda/(2\delta_2)$ are

$$a_1 \approx 0.67 (Re_1)^{\frac{1}{2}}. \tag{2.1}$$

$$T_2 \gamma \approx 0.18 (Re_1)^{\frac{1}{2}}. \tag{2.2}$$

The vorticity distribution in the asymptotic state is not in steady-state equilibrium, and will therefore undergo distortion by the array self-interaction. LC uses the asymptotic stretched state as initial conditions for numerical finite-difference solutions of the Navier–Stokes equations at $Re_2 = \Omega/\nu = O(500)$ ($Re_2 \approx \beta(L/\delta_1) Re_1$). These show collapse of the secondary vortices, perhaps via a strain-induced mechanism as described by Neu (1984 a, b), into nearly axially symmetric Burgers vortices of the type studied by Robinson & Saffman (1984). However for very large Re_2 this strong vortex self-interaction could be expected to influence the vortex evolution before the asymptotic state is attained, and indeed may play a crucial role in the secondary-vortex formation process itself. A self-consistent treatment of this question would seem to require a long-time, fully three-dimensional mixing-layer simulation (e.g. Couët and Leonard 1980) at realistic Re_1, over a streamwise domain containing perhaps the first two pairing events.

We shall suppose presently that in the limit of infinite Re_1, $Re_2(T_2 \to \infty)$, numerical simulations with zero fluid viscosity are of relevance to the dynamics of Corcos–Lin secondary vortices over the short stretching timescale γ^{-1}, prior to the onset of the viscous-diffusion stretching-strain vorticity balance which determines the Burgers vortex-sheet like asymptotic stretched state. In other words we shall assume that when $Re_2 \to \infty$, the early secondary vortex evolution will be dictated largely by the strong nonlinear interaction between the array self induction and the stretching strain. Further, in the present simple two-dimensional simulation, we shall model the switching on of the array self-induction at various stages of the formation process only by covering a range of different initial vortex geometries (i.e. δ_ω) and strengths (i.e. β). The result is rudimentary models of secondary-vortex evolution different in detail but with common features. In particular we find rapid deformation of initially eccentric Corcos–Lin vortices into spiral structures. For very large but finite Re_2 we might expect that the mode of viscous decay for these structures would be qualitatively similar to that found by Lundgren (1982) from solutions of the Navier–Stokes equations for the evolution of axially strained spiral vortices (see also Moore & Saffman 1973; Kaden 1931). In utilizing these solutions to model the fine structure of inertial-range turbulence, Lundgren finds decay on two distinct timescales; a short one on which individual spiral turns merge together forming an essentially inviscid, smoothed rotational vortex core, and a long timescale on which this core itself relaxes towards the strain viscous-diffusion controlled, nearly axially symmetric Burgers vortex. Significantly the Lundgren model contains a natural lengthscale for the Kolmogorov length, namely the radial wavelength of the oscillating part of the vorticity field within a band of rapidly decaying spiral vortex

turns. We note that double timescale decay is typical of the viscous fluid dynamics of spiral vortices and serves to illustrate the highly non-uniform character of the large-Re_2 limit for this type of vorticity distribution.

3. The initial-value problem

3.1. *The vorticity field*

The model describes the interaction of an array of non-uniform vortices (the secondary vortices) with an applied stretching-strain field. In Cartesian (x, y, z)-coordinates the full unsteady velocity field **u** has components

$$u_x = V_x(x, y, t), \tag{3.1a}$$

$$u_y = V_y(x, y, t) - \gamma(t) y, \tag{3.1b}$$

$$u_z = \gamma(t) z. \tag{3.1c}$$

In (3.1) the terms containing $\gamma(t)$ are the uniform plane-strain field in the (y, z)-plane induced externally by the primary vortices and V_x, V_y are the components of the self-induced velocity field of the secondary vortices. Referring to figure 1(*b*), z is directed locally along the braid of the nominally two-dimensional primary-vortex motion, x lies in the spanwise direction and y is normal to (x, z). The only non-zero component of the vorticity field is

$$\omega_z(x, y, t) = \frac{\partial V_y}{\partial x} - \frac{\partial V_x}{\partial y}. \tag{3.2}$$

The velocity and vorticity fields of (3.1) and (3.2) are such that vortex lines are of infinite extent and are always parallel to the z-axis. We assume that the fluid is incompressible, inviscid, and of constant density. On the (x, y)-plane projection of particle paths of (3.1), $x[x(0), t], y[y(0), t]$, it may be readily shown that for $\gamma(t) > 0$ the uniform plane-strain field amplifies ω_z as (Lundgren 1982; Jacobs & Pullin 1985)

$$\omega_z\{x[\ldots], y[\ldots], t\} = \omega_z\{x(0), y(0), 0\} \exp[Q(t)], \tag{3.3}$$

where

$$Q(t) = \int_0^t \gamma(t') \, dt'. \tag{3.4}$$

The secondary vortices are modelled here as an infinite x-wise periodic array consisting of one row of identical vortices with centroids at $y = 0$, $x = (p + \frac{1}{4})\lambda$, $p = -\infty, \ldots, \infty$ and circulation $-\Omega$, and of a second row of identical vortices with centroids at $y = 0$, $x = (p - \frac{1}{4})\lambda$, $p = -\infty, \ldots, \infty$ and circulation Ω. Figure 2 shows two members of the array corresponding to $p = 0$, which we denote by vortex 1 (right-hand side) and vortex 2 (left-hand side) respectively. Geometrically vortex 2 is the mirror image of vortex 1 in $x = 0$, and it has circulation equal in magnitude but opposite in sign to that of vortex 1. At time t each vortex appears in (x, y)-cross-section as a nested set of $M = 4$ non-intersecting contours which delineate discontinuities in the piecewise-constant ω_z field. We denote the contours of vortex 1 by the counterclockwise running curves $C_j(t)$, counting $j = 1, \ldots, M$ from the outermost contour inwards. The domain of the (x, y)-plane bounded by $C_j(t)$ and $C_{j+1}(t)$ is denoted by $R_j(t)$ and has area $A_j(t)$. $R_M(t)$ is interior to $C_M(t)$ and $R_0(t)$, $0 \leqslant x \leqslant \frac{1}{2}\lambda$ is exterior to $C_1(t)$. The initial vorticity distribution for vortex 1 is

$$\omega_z(x, y, 0) = \begin{cases} \omega_0(0) = 0 & \text{in } R_0(0), \\ \omega_j(0) = \text{const} & \text{in } R_j(0) \quad (j = 1, \ldots, M). \end{cases} \tag{3.5}$$
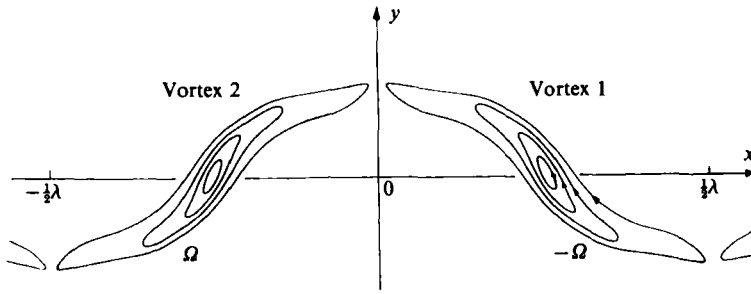
FIGURE 2. Pair of counter-rotating vortices in (x, y)-plane. The contours describing vortex 1 are $C_j, j = 1, 4$, where $j = 1$ for the outermost contour. $\omega_j(0)$ is the initial uniform vorticity in R_j bounded by C_j and C_{j+1}. The flow is irrotational outside of the vortices.

Hence from (3.4), for $t > 0$

$$\omega_z(x, y, t) = \omega_j(t) \quad \text{in } R_j(t), \tag{3.6a}$$

$$\omega_j(t) = \omega_j(0) \exp[Q(t)] \quad (j = 1, ..., M). \tag{3.6b}$$

Also
$$A_j(t) = A_j(0) \exp[-Q(t)], \tag{3.7}$$

$$\Omega_j = \omega_j(t) A_j(t) = \omega_j(0) A(0), \tag{3.8}$$

where Ω_j is the magnitude of the circulation contained in R_j. The $\Omega_j, j = 1, ..., M$ are invariants of the vortex motion and $\Omega = \Sigma_j \Omega_j$ is the magnitude of the total circulation of vortex 1.

3.2. *Contour-dynamics formulation*

The assumed vorticity structure allows use of the contour-dynamics (CD) method (Zabusky *et al.* 1979; Pullin 1981; Overman & Zabusky 1982) for the numerical simulation of the vortex-array evolution. In the present application, owing to the symmetries and periodicity of the system, it is only necessary to consider the motion of vortex 1 in figure 2. Let $\zeta_j(e, t) = x_j(e, t) + iy_j(e, t)$ $(j = 1, ..., M$ and $i^2 = -1)$, denote the coordinates of a particle on $C_j(t)$, where e is a contour parameter. Adapting the CD formulation of Jacobs & Pullin (1985) for uniform stretching vortices to the present configuration gives an initial-value problem for $\zeta_j(e, t)$ (an overbar denotes the complex-conjugate) as

$$\frac{\partial \bar{\zeta}_j}{\partial t} = i\gamma y_j + \frac{\exp[Q(t)]}{2\lambda i} \sum_{m=1}^{M} \Delta\omega_m \oint_{C_m} (y_j - y'_m) \left\{ \cot\left[\frac{\pi}{\lambda}(\zeta_j - \zeta'_m)\right] \frac{d\zeta'_m}{de'} \right.$$

$$\left. - \cot\left[\frac{\pi}{\lambda}(\zeta_j + \bar{\zeta}'_m)\right] \frac{d\bar{\zeta}'_m}{de'} \right\} de' \quad (j = 1, ..., M), \tag{3.9}$$

where $\Delta\omega_m = \omega_m(0) - \omega_{m-1}(0)$, $\zeta_j \equiv \zeta_j(e, t)$ and $\zeta'_m \equiv \zeta_m(e', t)$, $m = 1, ..., M$. The left-hand side of (3.9) expresses $u_x - iu_y$ defined in (3.1) for a material point on C_j, in terms of the instantaneous shapes of all the contours C_m, $m = 1, ..., M$. On the right-hand side of (3.9) the first term is the contribution of the stretching-strain field to the complex velocity and the integral terms are the self induction of vortex 1 and vortex 2 plus the relevant velocity contributions from all other members of the array. Note that when $e' \to e$ on C_j, the first of the two integrands in the integral in (3.9) take the value $2\partial y_j/\partial e$. The essential steps leading to (3.9) are outlined in Appendix A.

3.3. *Energy of the vortex array*

We define a measure of the energy of the array per member (i.e. energy of vortex 1) in the (x, y)-plane as

$$E(t) = \frac{1}{2} \int_0^{\frac{1}{2}\lambda} \int_{-\infty}^{\infty} (\nabla \psi)^2 \, dy \, dx, \tag{3.10}$$

$$V_x = -\frac{\partial \psi}{\partial y}, \quad V_y = -\frac{\partial \psi}{\partial x}, \tag{3.11}$$

where ψ is a stream function which satisfies $\nabla^2 \psi = -\omega_j(t)$ in $R_j, j = 0, \ldots, M$. Defining $\psi = 0$ on $x = \pm\frac{1}{2}\lambda$ and for $y \rightarrow \pm\infty$, using Green's first and second theorem and the planar Stokes theorem, (3.10) may be written, after some algebra as

$$E(t) = -\frac{1}{2}\exp\left[Q(t)\right] \sum_{m=1}^{M} \Delta\omega_m \oint_{C_m} \left[\psi \frac{\partial(\frac{1}{2}y^2)}{\partial n} - \frac{1}{2}y^2\left(\frac{\partial\psi}{\partial n}\right)\right] ds$$

$$+ \frac{1}{12}\exp\left[2Q(t)\right] \sum_{m=1}^{M} \Delta\omega_m[\omega_m(0) + \omega_{m-1}(0)]\oint_{C_m} y^3 \, dx, \tag{3.12}$$

where s is the arc length and n is the inward facing normal on C_m. The integral containing ψ may be further reduced to a form convenient for numerical integration, through integration by parts. For $\gamma(t) = 0$, $E(t)$ is an invariant of the vortex evolution, but for $\gamma > 0$, E may be expected to increase due to energy transfer from the strain field (first-order motion) to kinetic energy of the secondary vortices in the (x, y)-plane.

4. Numerical solution

For the present simulations, all physical quantities are made dimensionless against the length and timescales $\lambda/2\pi$ and $\lambda^2/(4\pi^2\Omega)$ respectively. This is equivalent to putting $\lambda = 2\pi$, $\Omega = 1$ in previous equations, and regarding all other quantities as dimensionless. Unless otherwise specified this will be the convention followed subsequently. The numerical method is generally similar to the CD code described by Jacobs & Pullin (1985) with improvements and refinements required for the larger-scale computations described here. Briefly the $C_j(t)$ are defined as a set of $N_j(t)$ nodes numbered $k = 1, \ldots, N_j(t)$. A suitable approximation to the integrals in (3.9) then leads to a set of $2N(t)$ ordinary differential equations (ODEs),

$$N(t) = \sum_{j=1}^{M} N_j(t)$$

for the node coordinates $\{[(x_j)_k, (y_j)_k], \ k = 1, \ldots, N_j(t)\}, j = 1, \ldots, M = 4$. There are three essential parts of the calculation; (i) evaluation of the integrals, (ii) timewise integration of the ODEs, (iii) numerical control of node distribution by use of a node insertion/deletion scheme, introduced so as to automatically provide adequate resolution in portions of the C_j where fine structure is generated locally.

For the calculation of the integrals, following a transformation of the form $\zeta^* = \exp\left[-i\zeta\right]$, each $C_j(t)$ was divided into elements defined on node subsets $[(\zeta_j^*)_{k-1}, (\zeta_j^*)_k, (\zeta_j^*)_{k+1}]$, $k = 2, 4, \ldots, N_j(t)$ by fitting a quadratic to $\zeta_j^*(e)$ in $k-1 \leqslant e \leqslant k+1$. The element contributions to the integral in (3.9) were then evaluated using a four-point Gaussian integration formula. Most of the simulations discussed here were also performed using Simpson's rule on each element with
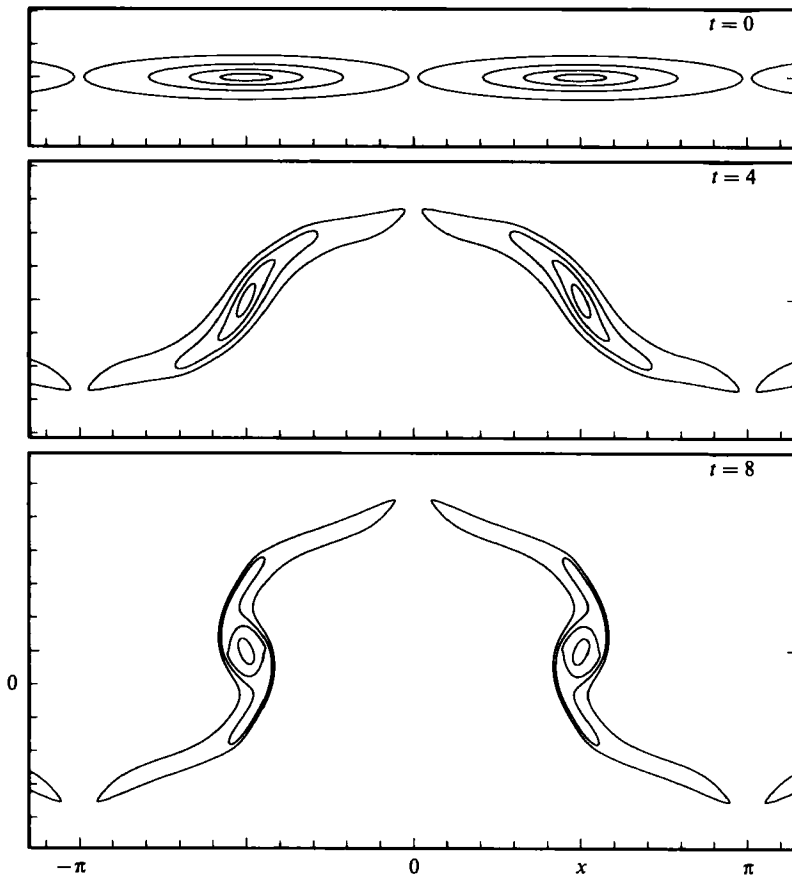
FIGURE 3. For caption see facing page.

integration variable $e \equiv k$. Although these two schemes produced identical $C_j(t)$ shapes to the accuracy of the large-scale plots discussed subsequently, the Gaussian method gave better smoothness properties for the $C_j(t)$ on the node-spacing scale, during the latter part of the computation.

The ODEs obtained from (3.9) were integrated using a fourth-order Runge–Kutta–Fehlberg method. The algorithm contained automatic control of the timestep $\Delta t_1(t)$, set locally such that the single-step truncation error did not exceed a user-specified tolerance $\epsilon^{(1)}$, with $\epsilon^{(1)} = 10^{-4}$ here.

The node insertion procedure is a refinement of that used by Jacobs & Pullin (1985). Full details and some discussion are given in Appendix B.

The accuracy of the calculations was checked by:

(a) monitoring variations of the fractional error in the circulation invariants.

$$\delta(\Omega_j) \equiv \frac{\Delta\Omega_j(t)}{\Omega_j(0)} = \frac{[\exp(\hat{\gamma}t) A_j(t) - A_j(0)]}{A_j(0)}, \qquad (4.1)$$

where $A_j(t)$ is the calculated area of $R_j(t)$ and $\hat{\gamma}$ is the constant dimensionless strain rate;

(b) observing changes in the energy invariant (3.13) for calculations with $\hat{\gamma} = 0$;

(c) the use of different spatial and timewise integration procedures in test cases for the purposes of checking the sensitivity of the results to variations in the details of the numerical technique.
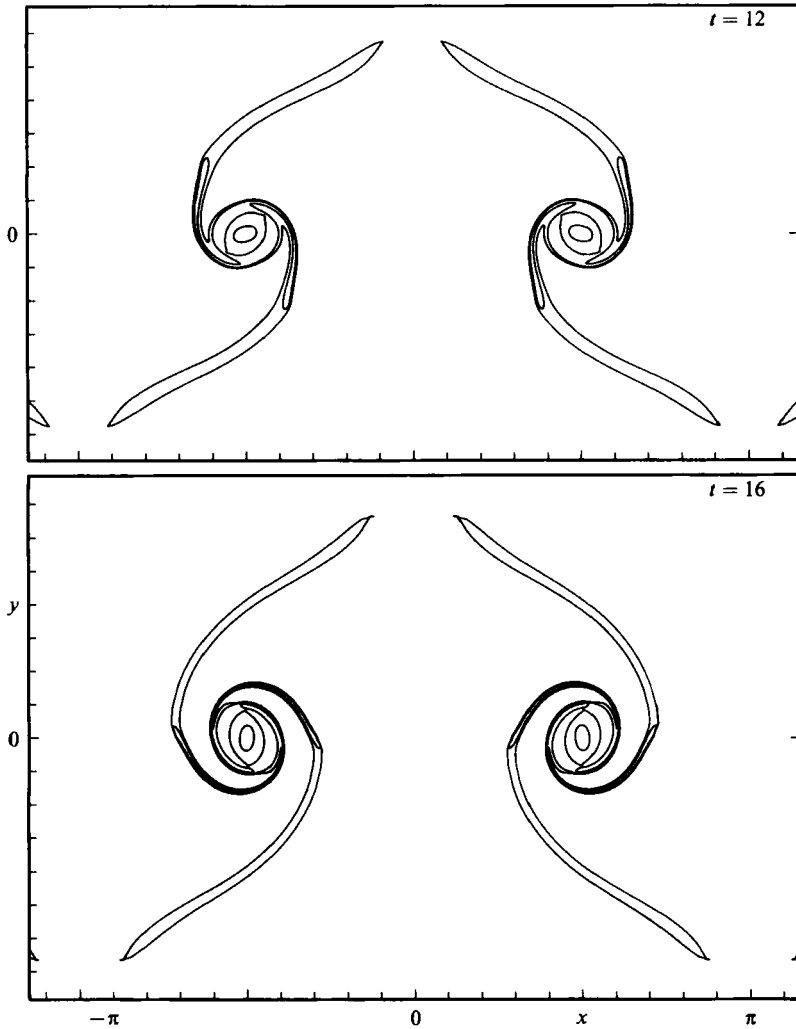
FIGURE 3. Evolution of vortex array, $a_2 = 12.7$, $\hat{\gamma} = 0$. Dimensionless times t as shown.

5. Initial conditions and parameters

The initial conditions refer to the geometrical shape of the C_j and the values of the $\omega_j(0), j = 1, ..., 4$. Each C_j was initially elliptically shaped, as illustrated for example in the first frame of figure 3. The dimensions of the major and minor ellipse axes $(r_1)_j$ and $(r_2)_j$ respectively, and the values of $\omega_j(0)$ were chosen to model a nearly sinusoidal distribution of vorticity along $y = 0$, and a normal vorticity distribution along $x = \pm\frac{1}{2}\pi$. We define the initial vorticity thickness δ_ω for each vortex as

$$\delta_\omega = \frac{2 \sum\limits_{j=1}^{4} \omega_j(0)[(r_2)_j - (r_2)_{j+1}]}{\omega_{max}}, \tag{5.1}$$

where $(r_2)_5 = 0$ and $\omega_{max} = \omega_4(0)$. The vortex aspect ratio is defined as $a_2 = \pi/\delta_\omega$. Since the formation mechanism that initially produces the secondary vortices is not fully understood, their strength and typical geometry at the time when nonlinear self-interaction begins to influence their evolution remains uncertain. Hence we

C_j	$(r_1)_j$	$a_2 = 12.7$		$a_2 = 25.8$		$a_2 = 51.7$	
		$(r_2)_j$	$\omega_j(0)$	$(r_2)_j$	$\omega_j(0)$	$(r_2)_j$	$\omega_j(0)$
C_1	1.53	0.208	-0.63	0.102	-1.29	0.0512	-2.57
C_2	0.918	0.125	-1.48	0.0612	-3.02	0.0306	-6.037
C_3	0.535	0.0728	-2.00	0.0357	-4.08	0.01785	-8.159
C_4	0.247	0.0336	-2.30	0.0165	-4.69	0.00824	-9.382

TABLE 1. Initial geometry and vorticity distribution for vortex 1 of figure 2, for three initial vortex geometries. Values of δ_ω are 0.248, 0.122 and 0.0608

considered three initial configurations corresponding to $a_2 = 12.7$, 25.8 and 51.7, and several values of $\hat{\gamma}$. The respective ellipse and vorticity parameters are summarized in table 1. The initial number of nodes distributed on C_1 were $N_1(0) = 60$ $(a_2 = 12.7)$, $N_1(0) = 60$ $(a_2 = 25.8)$ and $N_1(0) = 100$ $(a_2 = 51.7)$. Proportionally smaller $N_j(0), j = 2,3,4$ were used on the inner ellipses. The only further parameter is $\hat{\gamma} = \gamma\lambda^2/(4\pi^2\Omega)$, which is related to the LC parameter $\hat{\Omega} = \Omega/(\gamma\lambda^2)$ as $\hat{\gamma} = (4\pi^2\hat{\Omega})^{-1}$. Using $\gamma \approx \pi U/(2L)$, $\lambda \approx L$ and $\Gamma \approx UL$, for secondary vortices in a mixing layer gives $\hat{\gamma} \approx (8\pi\beta)^{-1}$ where $\beta = \Omega/\Gamma$. The hot-wire measurements of Jimenez (1983) (see also Jimenez *et al.* 1985) indicate $\beta = O(1)$. Using $\beta = 0.25$ and 0.5 gives $\gamma \approx 0.16$ and 0.08 respectively. Here we take $\hat{\gamma} = 0$, 0.1, 0.2 and 0.4. This last value is large but is of interest as an extreme case.

6. Results and discussion

Sequences of evolving contour portraits which depict the timewise deformation of a typical vortex pair for the range of a_2 and $\hat{\gamma}$ treated are shown in figures 3–4 and 7–20. We regard the simulations as quantitatively reliable for $0 \leqslant t \leqslant t_{max}$ where, for most cases displayed, t_{max} is a value somewhat larger than those indicated in the final frame of each sequence. Individual calculations were generally terminated for $t \geqslant t_{max}$ when either (i) $\max_j[\delta(\Omega_j)] \geqslant \epsilon^{(2)}$, where $\epsilon^{(2)} = O(10^{-2})$ and/or (ii) $\max_j[N_j(t)] \geqslant N_{max}$, where the value $N_{max} = 1000$ was determined by available computing resource limitations. The onset of (i) was usually accompanied by the appearance of substantial spatial oscillations in the shape of the C_j on the order of the local node spacing, which was taken to indicate insufficient local resolution. $\max_j[N_j(t)]$ invariably occurred on C_1, with a typical value of 600 and $\Sigma_j N_j(t) \sim O(1500)$.

Figures 3 and 10 show the array evolution with $\hat{\gamma} = 0$, (i.e. no out-of-plane stretching) for $a_2 = 12.7$ and $a_2 = 25.8$ respectively. These cases are of interest since first they provide solutions against which the influence of $\hat{\gamma} > 0$ can be evaluated, and secondly, variations in $E(t)$ given by (3.12) may be used as a global check on accuracy. At $t = 4$ in the sequence of figure 3, the differential rotation of the C_j induced by the initial vorticity concentration towards the centre of each vortex is clearly evident. Later, for $t \geqslant 12$, this results in the formation of a central vortex core. Simultaneously, the vortex tails (those regions of the initial vortex closest to neighbouring vortices) are drawn out into thin, curved vortex layers whose thickness is small compared to the local radius of curvature. The overall result by $t = 16$ is the generation of a rolled-up double spiral vortex not unlike those found in vortex coalescence computations (Zabusky *et al.* 1979; Overman & Zabusky 1982; Jacobs
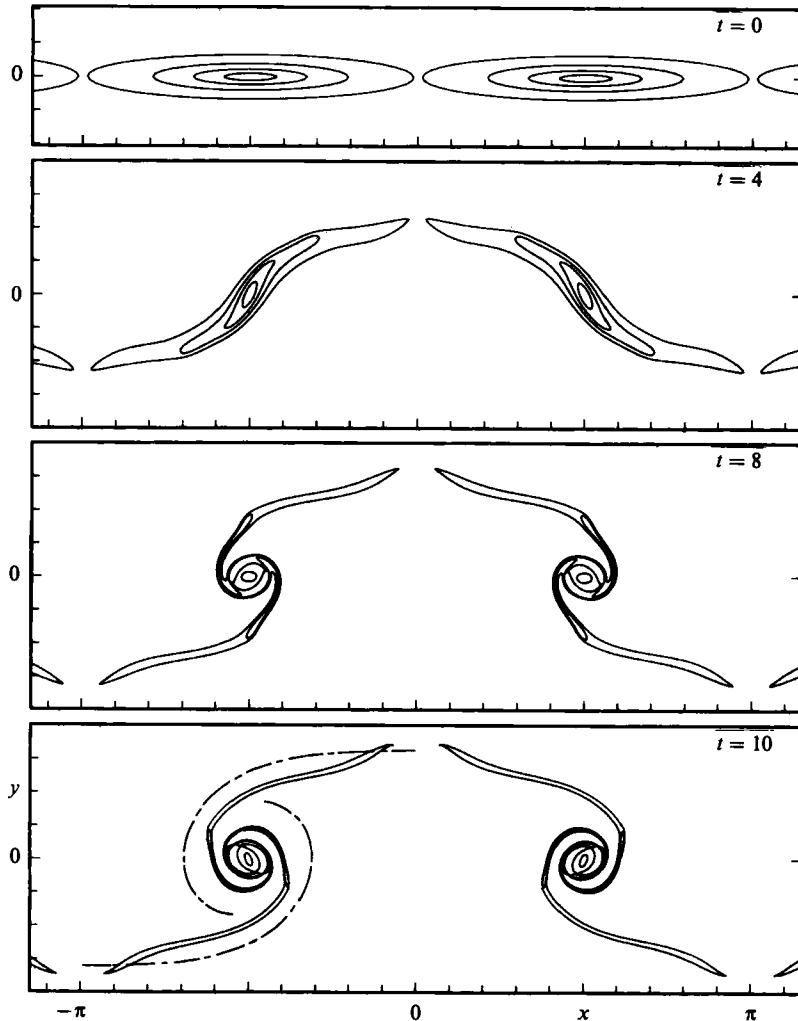
FIGURE 4. Evolution of vortex array, $a_2 = 12.7$, $\gamma = 0.1$. Dot-dashed lines show the (x, y)-plane projection of the stagnation stream surface for a point-vortex approximation to the secondary array. Dimensionless times t as shown.

& Pullin 1985). Note that the inner contours C_3 and C_4, which contain roughly 25 % of Ω at $t = 16$ in figure 3, quickly collapse into the vortex core. In contrast the outer contours C_1 and C_2 undergo continuous and large deformation both within the vortex core and as part of the spiral filament, resulting in large vorticity gradients on the outer edge of the core.

The sequence of figure 4 with $a_2 = 12.7$, $\hat{\gamma} = 0.1$ shows the expected exponential reduction in the $A_j(t)$ as vortex lines are stretched longitudinally by the z-component of the strain. With $\hat{\gamma} = 0.2$ and 0.4 in figures 7 and 8 respectively, the increased spin induced by the vorticity amplification is strong enough to substantially reduce the timescale of the initial vortex core roll-ups, when compared with the $\hat{\gamma} = 0$ evolution. By analogy with the roll-up of the primary shear layer, we assume that the dimensional roll-up timescale for $\hat{\gamma} = 0$ is order λ/σ_0 where σ_0 is the velocity jump across the flattened vortex at its centroid at $t = 0$. Using a vortex-sheet model with $\sigma(x) = \sigma_0 \sin{(2\pi x/\lambda)}$, where $\sigma_0 = \pi\Omega/\lambda$, in conjunction with a similarity transforma-
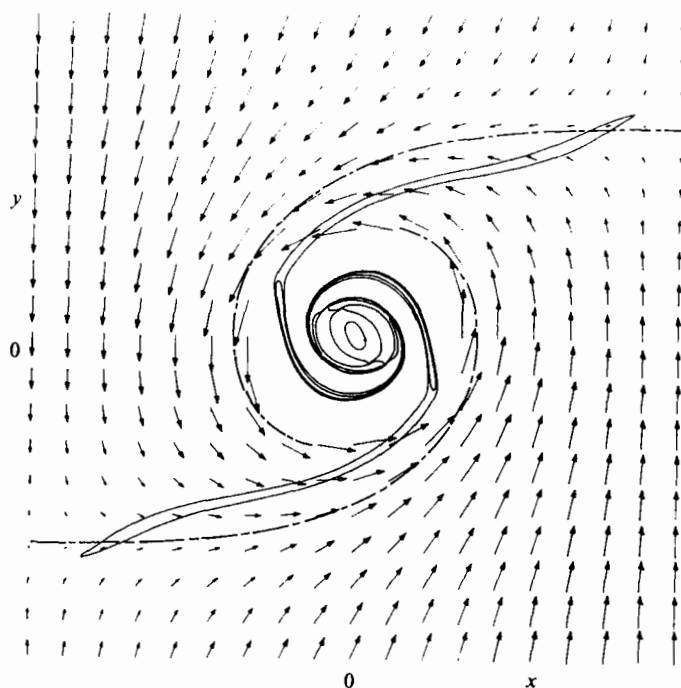
FIGURE 5. Magnified view of vortex contours, $a_2 = 12.7$, $\hat{\gamma} = 0.1$, $t = 10.0$. Arrows indicate the (x, y)-velocity field of a point-vortex array in the (y, z)-plane stretching-strain field with $\hat{\gamma} = 0.1$. Dot-dashed lines represent the (x, y)-projection of the stagnation stream surface for this velocity field.

tion (Lundgren 1982) which relates stretched and equivalent unstretched two-dimensional vortex flows, we estimate the dimensionless roll-up timescale for $\hat{\gamma} > 0$ as $\hat{T}_3 \approx \hat{\gamma}^{-1} \ln(1 + 4\pi\hat{\gamma})$, in broad agreement with the trends shown in figures 3–4 and 7–8. In figure 8 at $t = 5$, the beginning of a local shear instability may be seen on each flattened spiral vortex arm. This instability occurs at the tip of C_2 presumably because of the contour shape perturbations caused locally by the vorticity gradient along the vortex sheet. Thus the actual site of the local instability is determined by the artificial and non-smooth character of the piecewise-constant vorticity field. However a continuous initial vorticity field will generally contain local non-uniformities qualitatively similar to those modelled here by vorticity discontinuities and hence the appearance of local or tertiary instabilities dynamically equivalent to those produced in our simulations may be expected.

The trend of the simulations with $a_2 = 25.8$ ($\hat{\gamma} = 0$, 0.1, 0.2, 0.4) in figures 10–16 and with $a_2 = 51.7$ ($\hat{\gamma} = 0.1$, 0.2) in figures 17–20 shows some resemblance to those for $a_2 = 12.7$ but with notable differences in detail. The more-flattened initial vortex shape leads to enhancement of shear instability. In some cases, for example as in figures 14 and 17 these local instabilities are dominant to the extent that each vortex evolution is perhaps best viewed as a series of local roll-ups of the type that were shown by LC (§4) to evolve on infinite, stretched shear layers subject to periodic streamwise perturbations. These (tertiary) vortex cores are connected by their own system of thin braids, each undergoing biaxial stretching caused by the combined strain fields of the primary and secondary vortices. By analogy with the (uncertain) formation mechanism for the secondary vortices, we might speculate that this new
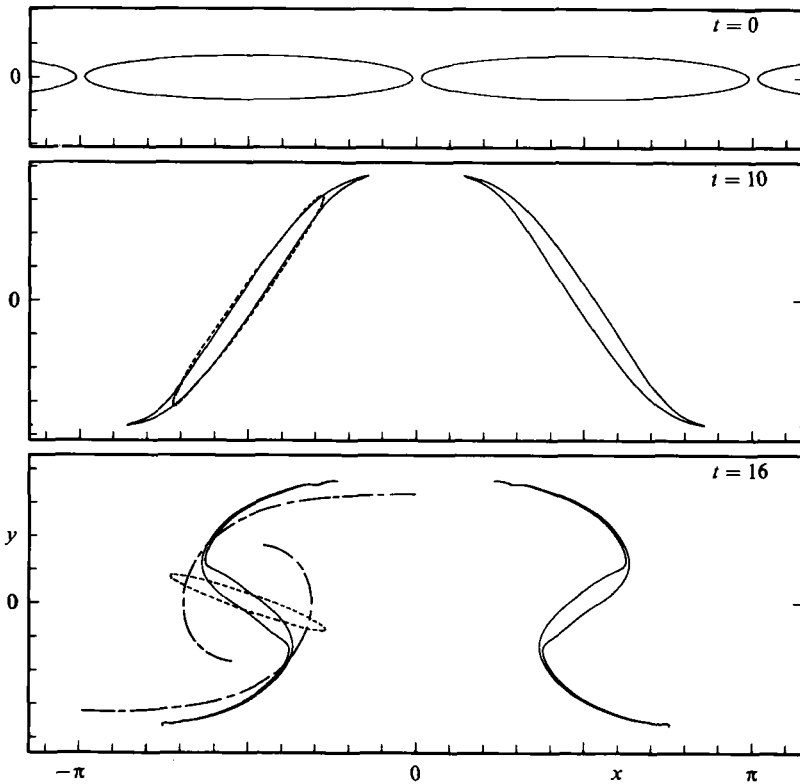
FIGURE 6. Evolution of vortex array, $a_2 = 8$, $\hat{\gamma} = 0.1$. The vorticity is uniform in each vortex. Dashed contours indicate the evolution of an isolated elliptical vortex embedded in a (y, z)-plane stretching strain field $\hat{\gamma} = 0.1$.

braiding system may provide sites for the production of still higher-order structure orthogonal to and acting as an energy sink to the secondary vortices.

When $a_2 \to \infty$, the secondary-vortex array may be viewed as an initially flat vortex sheet with a sinusoidal strength distribution. This limit has been studied analytically by Neu (1984b) who demonstrated strain-induced collapse to a point vortex of isolated segments of vortex sheets with initially elliptical strength distributions. There is now evidence (e.g. Meiron, Baker & Orszag 1982) that indicates that an unstretched vortex sheet of uniform strength develops a singularity in a finite time t_c following an initial shape or strength perturbation. The sheet evolution for $t \geqslant t_c$ remains an open question, but may locally take the form of a double-arm similarity spiral of the type studied by Pullin & Phillips (1981). The stretched or unstretched vortex sheet with sinusoidal strength variation has received little attention numerically. Possible behaviour including singularity/vortex-spiral production modified by the Neu collapse mechanism may elucidate the large aspect-ratio limit for the dynamics of secondary vortices with initially smooth vorticity distributions.

In figures 9, 12, 15–16, 18 and 19 we show magnified views of the vortex core region at selected times, which illustrate the fine structure of the vorticity field. Shown inset in figures 9 and 12 are vorticity distributions obtained along cuts through the vortex centroid. Notice the reversal in sign of the vorticity gradient produced near the outer edge of the core by 'roll-up' of C_3 interior to the vortex. On a long timescale we would expect that the accelerating differential rotation in the vortex core would wind these
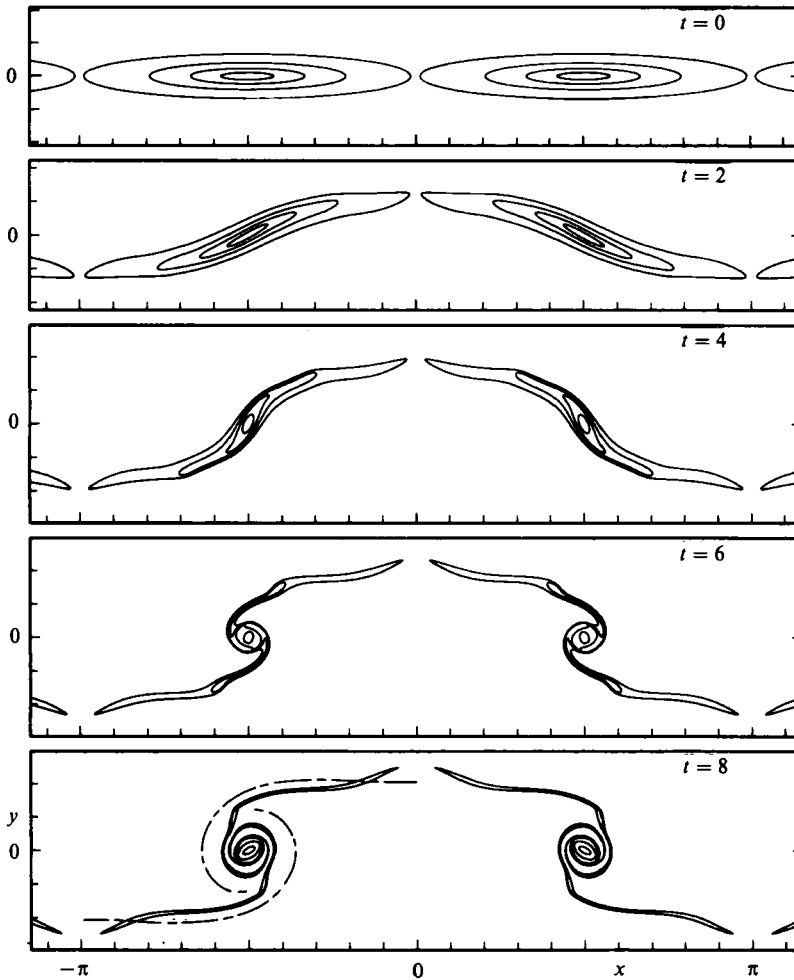
FIGURE 7. Evolution of vortex array, $a_2 = 12.7$, $\hat{\gamma} = 0.2$. Dimensionless times t as shown.

gradient reversals into a spiral embedded within weaker ambient core vorticity, thus producing even finer scales of motion than those generated on the 'outer' spiral.

The details of figures 16 and 19 reveal corrugations of the C_j on the scale of the local node spacing which are not visible in the corresponding larger-scale plots of figures 14 and 17 respectively. This is a purely numerical instability which signals the breakdown of the computation. It appears because the node insertion/deletion scheme is ultimately unable to provide, within the bound $\max[N_j(t)] \leqslant N_{max}$, the small-scale node spacing required for the resolution of the very finest scales of motion. For figure 16 we find $\delta(\Omega_1) \approx 0.003$, $\delta(\Omega_2) \approx 0.01$, $\delta(\Omega_3) \approx 0.04$, $\delta(\Omega_4) \approx 0.08$ (see (4.3)) at $t = 3.8$ while for figure 19 we find $\delta(\Omega_1) \approx 0.005$, $\delta(\Omega_2) \approx 0.01$, $\delta(\Omega_3) \approx 0.003$, $\delta(\Omega_4) \approx 0.1$ at $t = 3.8$. For these extreme cases (i.e. large a_2) these values indicate that the respective solutions are losing quantitative accuracy, and that they provide only a qualitatively faithful picture of the tendency towards the formation of a series of vortex cores through local instabilities. In figure 19 we indicate the division of the vortex into core and braid segments at $t = 3.8$. The respective fractions of the total circulation in each segment are $\Omega_A \approx 0.11\Omega$, $\Omega_B \approx 0.07\Omega$, $\Omega_C \approx 0.035\Omega$, $\Omega_D \approx 0.12$, $\Omega_E \approx 0.03\Omega$, $\Omega_F \approx 0.27\Omega$ and $\Omega = 2(\Omega_A + \Omega_B + \Omega_C + \Omega_D + \Omega_E) + \Omega_F$.
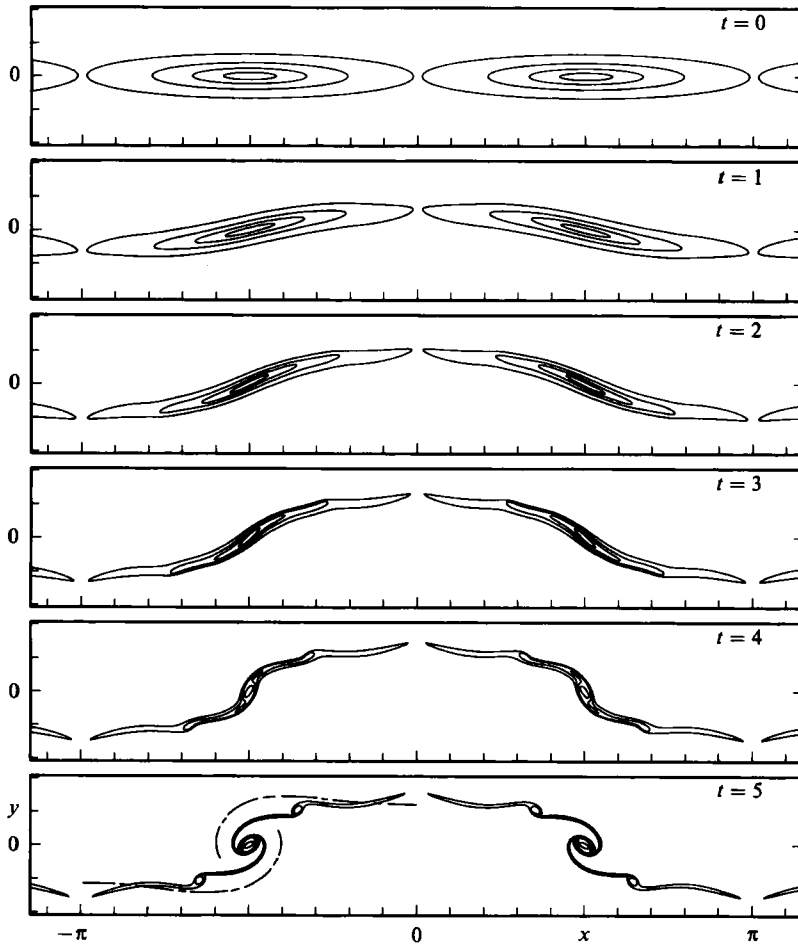
FIGURE 8. Evolution of vortex array, $a_2 = 12.7$, $\hat{\gamma} = 0.4$. Dimensionless times t as shown.

A comparison of the final frame of each simulation suggests that the vortex tails appear to approach a nearly stationary state. This may be understood as follows: in the vicinity of the vortex tails the dimensional velocity field may be well approximated by a point-vortex model obtained by assuming that the circulation $\pm \Omega$ of each finite-area vortex is concentrated at the vortex centroid. The (x, y)-plane velocity field for this point-vortex array coupled with the stretching strain is

$$u_x - \mathrm{i}u_y = \frac{\Omega}{2\lambda\mathrm{i}} \left\{ \cot\left[\frac{\pi}{\lambda}(x+\mathrm{i}y+\tfrac{1}{4}\lambda)\right] - \cot\left[\frac{\pi}{\lambda}(x+\mathrm{i}y-\tfrac{1}{4}\lambda)\right] \right\} + \mathrm{i}\gamma y. \qquad (6.1)$$

When $\gamma > 0$, (6.1) exhibits stagnation points on the planes of mirror symmetry at $x_m = \tfrac{1}{2}m\lambda$, $y_m = (-1)^m Y\lambda/(2\pi)$, $m = 0, 1, 2, \ldots$, where Y is a solution of

$$Y \cosh(Y) - (2\pi\hat{\gamma})^{-1} = 0. \qquad (6.2)$$

For $\hat{\gamma} = 0.1, 0.2$ and 0.4, $Y \approx 1.018, 0.652$ and 0.372 respectively. The dimensionless velocity field from (6.1) ($\Omega = 1, \lambda = 2\pi$) with $\hat{\gamma} = 0.1$ is shown in figure 5 superimposed on the contour shapes for $a_2 = 12.7$, $\hat{\gamma} = 0.1$ at $t = 10$ from figure 4. Also shown in figure 5 and in the final frame of each of figures 4, 6–8, 11, 13, 14, 17 and 20 are segments of the (x, y)-plane stagnation streamlines of (6.1) for the left-hand vortex (vortex 2). As the vortex tilts in the anticlockwise direction, it appears that the tips
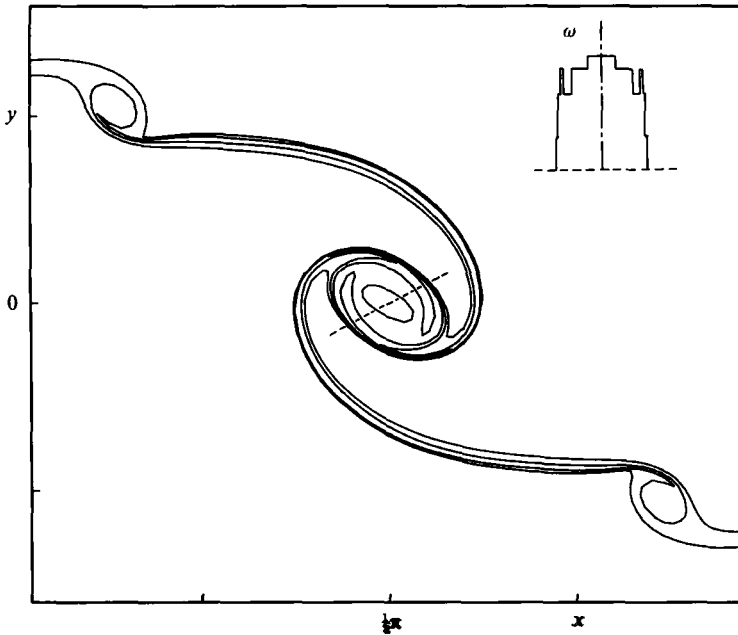
FIGURE 9. Magnified view of vorticity contours, $a_2 = 12.7$, $\hat{\gamma} = 0.4$, $t = 5$. Inset: vorticity distribution in vortex core.

of the flattened vortex tails nearly stagnate near the planes of mirror symmetry. Simultaneously the vortex core contracts in the presence of a local strain field which is the sum of the (y, z)-plane stretching strain, and the (x, y)-plane strain field induced near the vortex *centroid* by all other members of the array. These events combine to produce the conditions required to both generate and sustain the spiral structure. Within the model inviscid dynamics, the ultimate result indicated is a winding collapse of each vortex. The agreement with this model is less convincing for the $a_2 = 51.7$ results of figures 17 and 20 first because the point-vortex approximation loses accuracy near the vortex tails owing to the extended vortex geometry, and secondly since the simulation is terminated before the vortex tails have fully rotated into the stagnation region.

In figure 6 we show the vortex-array evolution calculated using a single-contour ($M = 1$) uniform-vorticity model. The total circulation and initial shape of C_1, and hence the mean vorticity is the same as the simulation of figure 4. By comparison we show also in figure 6 the evolution of an isolated uniform elliptical vortex subject to a (y, z)-plane stretching-strain field with $\hat{\gamma} = 0.1$. The initial aspect ratio and strength are as for the left-hand member (vortex 2) of the pair shown at $t = 0$, so that differences in the subsequent shapes may be attributed to the influence of the array on vortex 2. By $t = 10$ both vortex 2 and the isolated vortex have tilted and have changed their shape to some extent, but the array pair exhibit no fine structure remotely comparable to that depicted in the $t = 10$ frame of figure 4. At $t = 16$, which is beyond the range of the present non-uniform vortex computation, the vortices of figure 6 have decreased in both area and in effective aspect ratio. This is an example of the Neu (1984*a,b*) strain-induced collapse mechanism for isolated elliptical vortices, modified for vortex 2 by the (x, y)-plane strain of all other members of the array. LC gives an estimate of the collapse time for isolated vortices (LC, equation 3.8) by assuming collapse following a local balance between the self-induction
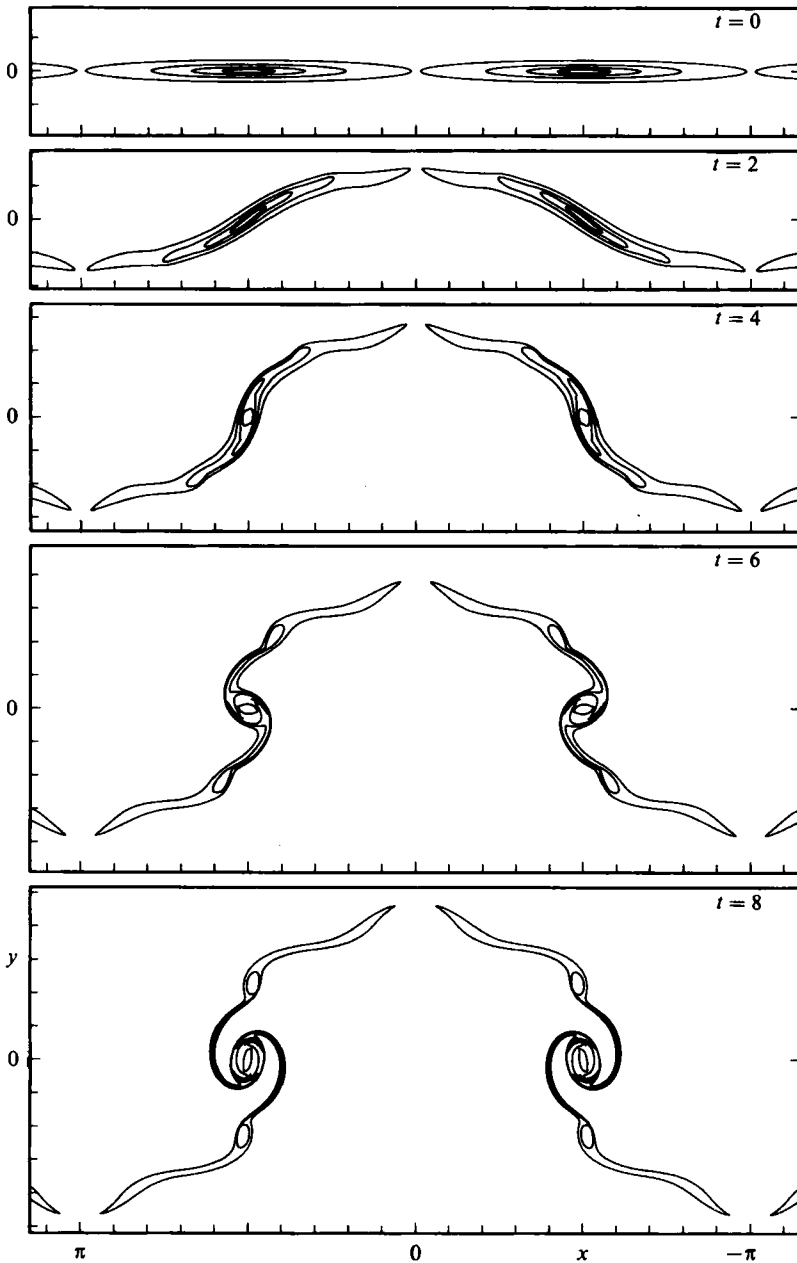
FIGURE 10. Evolution of vortex array, $a_2 = 25.8$, $\hat{\gamma} = 0$. Dimensionless times t as shown.

velocity at the vortex tip and the y-component of the strain velocity. In our notation, this is

$$\hat{T}_4 \approx 60(1+\eta)^4 \cos^2 \theta_e \, \hat{\gamma}, \qquad (6.3)$$

where η^{-1} is the ellipse aspect ratio and θ_e may be identified with the angle of tilt at $t = 10$ in figure 6. With the parameters of figure 6, $\hat{T}_4 \approx 7.5$ which is somewhat less than $\hat{T}_4 \approx 16$ suggested by the results of figure 6. For the present non-uniform vortex evolution, the collapse mechanism appears to be only partly effective, since the nonlinear self-induction of the flattened vortices generates a rolled-up and
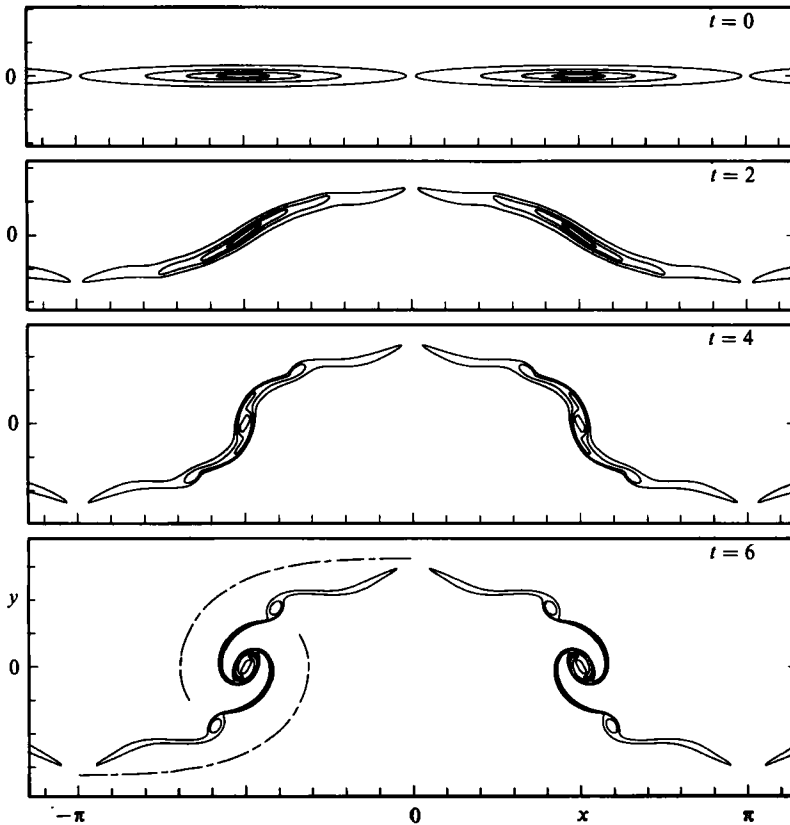
FIGURE 11. Evolution of vortex array, $a_2 = 25.8$, $\hat{\gamma} = 0.1$. Dimensionless times t as shown.

dominant vortex core before substantial local focusing of vorticity by the γ-component of strain can become operative. We note that this result appears to cast some doubt on the relevance of uniform-vortex models to the inviscid dynamics of non-uniform vortices, at least for those initial distributions that will produce a rapid distortion of the vorticity field.

In figures 21 and 22 we have plotted the energy associated with vortex-array-induced fluid velocities in the (x, y)-plane as calculated from (3.12) with $a = 12.7$ and 25.8 respectively. When $\hat{\gamma} = 0$, $E(t)$ is sensibly constant with errors $(E(t_{\max}) - E(0))/E(0) \approx 0.005$ in both cases. When $\hat{\gamma} > 0$, $E(t)$ increases because of energy transfer from the stretching-strain field to kinetic energy in the (x, y)-plane vortex motion. Further transfers to smaller scales given by the spiral-vortex turn spacing and by shear-layer instability scales may be expected but these transfers have not been resolved in quantitative detail here. In a real viscous fluid this energy is eventually dissipated in both the vortex-sheet and rod structures generated by the nonlinear vortex evolution.

A quantitative measure of individual-vortex deformation during its evolution is shown in figures 23–25, where we have plotted the perimeters of the nested vortex contours against t. In these figures both C_3 and C_4 show a sudden reduction near the time of formation of the central vortex core. By contrast C_1 and C_2 exhibit an explosive increase in length as they are advected into and undergo rapid distortion within the spiral vortex arms.
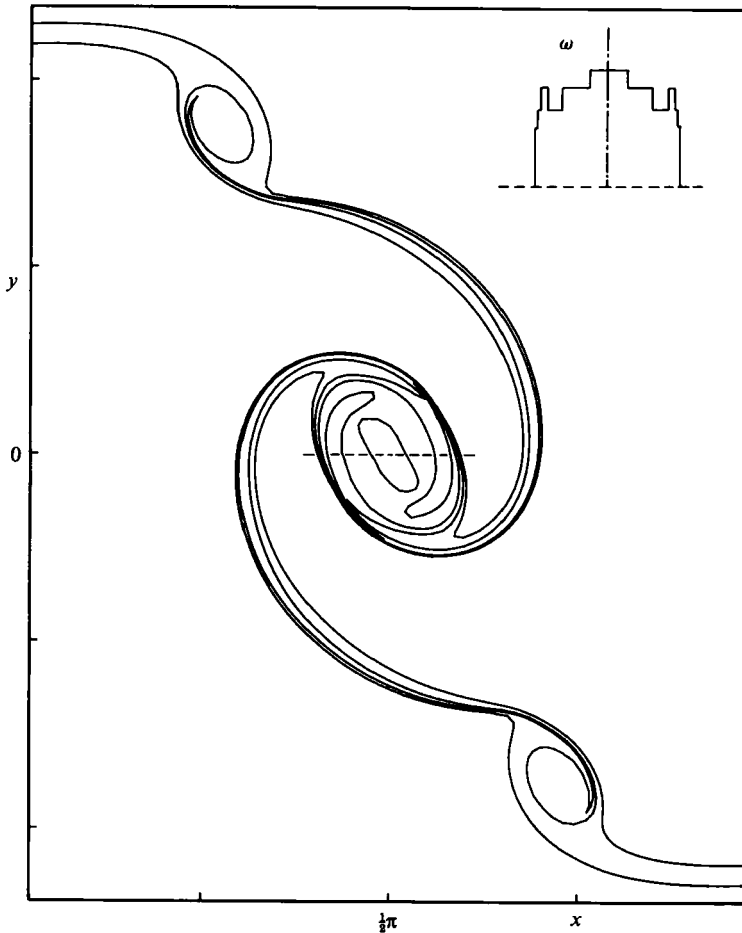
FIGURE 12. Magnified view of vortex contours, $a_2 = 25.8$, $\hat{\gamma} = 0.1$, $t = 6$. Inset: vorticity distribution in vortex core.

Lastly we discuss briefly the possibility of large-scale instability of the secondary-vortex array by pairing or other cooperative modes subsequent to the formation, for γ not too large, of compact vortex cores. This was found to a limited extent by LC for the post-roll-up phase of the perturbed Burgers vortex sheet (that is, within an individual flattened secondary vortex), but they did not consider possible pairing instabilities of the alternating-vortex array. A crude estimate of the timescale for two-dimensional cooperative instability is of interest, and can be obtained using simple point-vortex approximation. Consider a doubly infinite array of point vortices, with members of strength $-\Omega$ at $y = 0$, $x = (m + \frac{1}{4})\lambda$, $m = -\infty$, ..., ∞, and other members of strength Ω at $y = 0$, $x = (n - \frac{1}{4})\lambda$, $n = -\infty$, ..., ∞. Introducing perturbations to individual vortex coordinates proportional to $\exp[\sigma t + \mathrm{i}2\pi pq]$, $0 \leqslant p \leqslant 1$, where $q = m$ or n and following an argument given in Lamb (1932, Article 156), then a simple calculation shows that the growing mode of the perturbations has growth rate.

$$S = \frac{1}{2}\left[\left\{\gamma^2 + \frac{\Omega^2\pi^2}{\lambda^4}[(2p^2 - 2p + 1)^2 - (1 - 2p)^2]^2\right\}^{\frac{1}{2}} - \gamma\right]. \qquad (6.4)$$
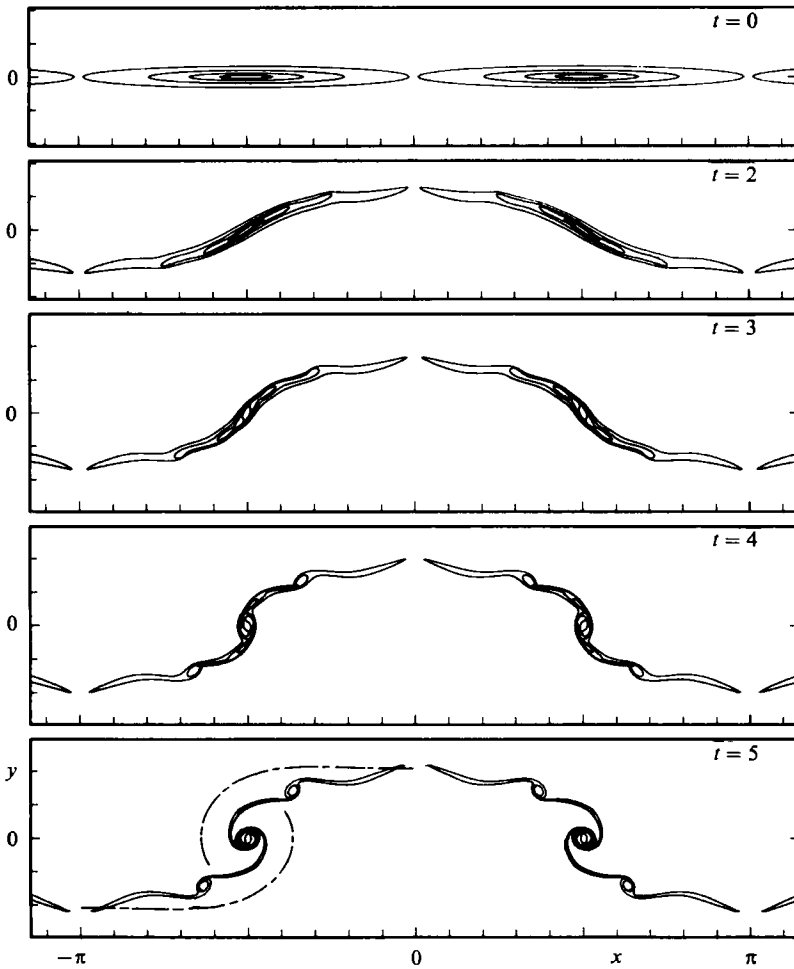
FIGURE 13. Evolution of vortex array, $a_2 = 25.8$, $\hat{\gamma} = 0.2$. Dimensionless times t as shown.

Hence stretching strain reduces but does not eliminate the instability. From (6.4), S is a maximum for $p = \frac{1}{2}$ corresponding to pairing; note that this may not be true for finite-area vortices (see Meiron, Saffman & Schatzman 1984). Using $\gamma = \pi U/(2L)$, $\Omega = \beta UL$, $p = \frac{1}{2}$, then the timescale $T_5 = S^{-1}$ for the pairing instability is

$$T_5 \gamma = 2[(1+\beta^2)^{\frac{1}{2}} - 1]^{-1}. \qquad (6.5)$$

Taking values of $\beta = 0.25, 0.5$ and 1.0 in (6.4) gives $T_5\,\gamma \approx 65$, 17 and 5 respectively. Hence, in the point-vortex approximation the timescale for the pairing instability is long compared to γ^{-1}, and this timescale may be thus expected to be long compared with the timescale required for the evolution of the fine structure of individual vortices seen in the present simulations. This result may be used to justify *a posteriori* the present imposed constraint, which by virtue of the mirror-image symmetry imposed on the vortex-pair geometry of figure 2, requires that the coordinates of the vortex centroids remain invariants of the evolution. We note that the rough estimate given above may be substantially altered by finite vortex area. Further there are three-dimensional instabilities of the array that may have larger growth rates than the two-dimensional pairing mode discussed above, which we have
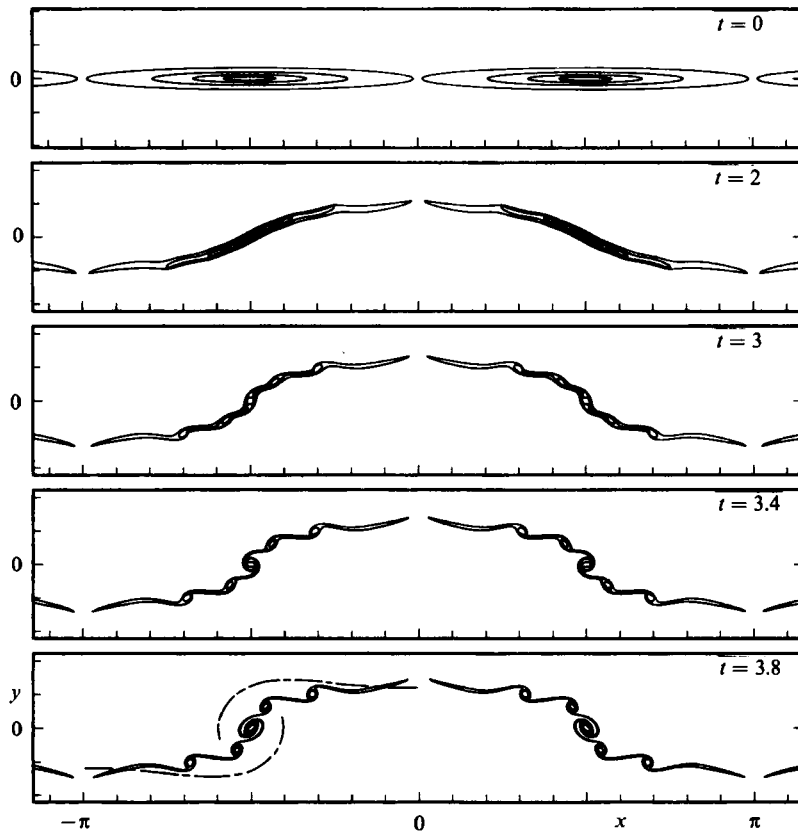
FIGURE 14. Evolution of vortex array, $a_2 = 25.8$, $\hat{\gamma} = 0.4$. Dimensionless times t as shown.

not considered here. These include the analogue for secondary vortices of the three-dimensional translative instability studied by Pierrehumbert & Widnall (1982), and the pinching instability, leading to vortex-ring-like structures, discussed by Jimenez (1983).

7. Conclusions

We have presented computations illustrating the nonlinear inviscid evolution of an array of Corcos–Lin secondary vortices in the presence of a longitudinal stretching-strain field. At values of the strain $\hat{\gamma}$ characteristic of the mixing layers, $0 < \hat{\gamma} \leqslant 0.2$, the vorticity field reveals fine details of the flow development which include:

(i) the rapid formation of an intense rolled-up vortex core with companion double-arm vortex spirals;

(ii) incipient tertiary instabilities embedded within spiral filaments, and containing in some case their own smaller-scale vorticity spirals;

(iii) the presence of weak sheet-like vorticity tails terminating the spirals, which are maintained by the local (x, y)-plane velocity field generated near each vortex tail by the combined velocity induction of all members of the secondary-vortex array coupled with the y-component of the strain velocity.

There are many features of real mixing-layer flows that we have of necessity neglected in the present model. These include the timewise decay of the stretching
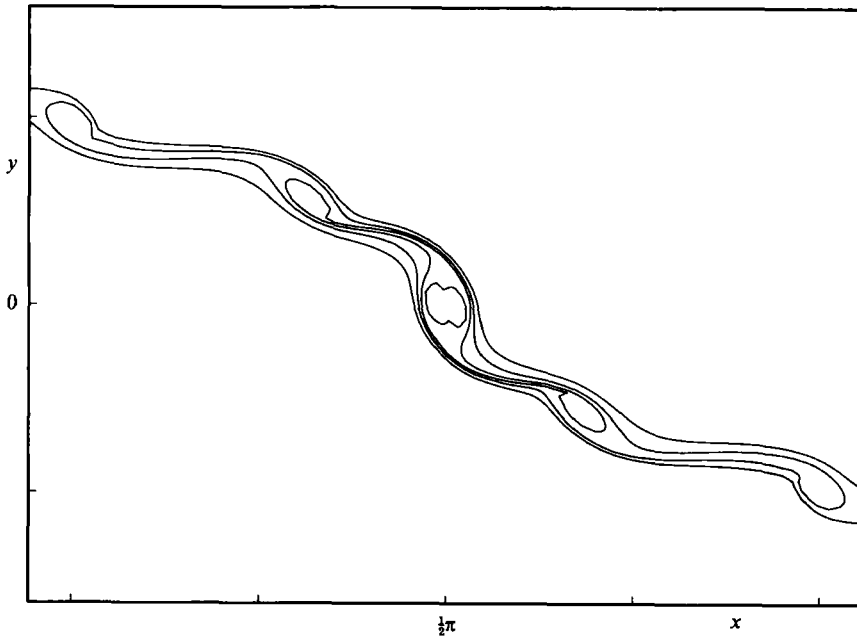
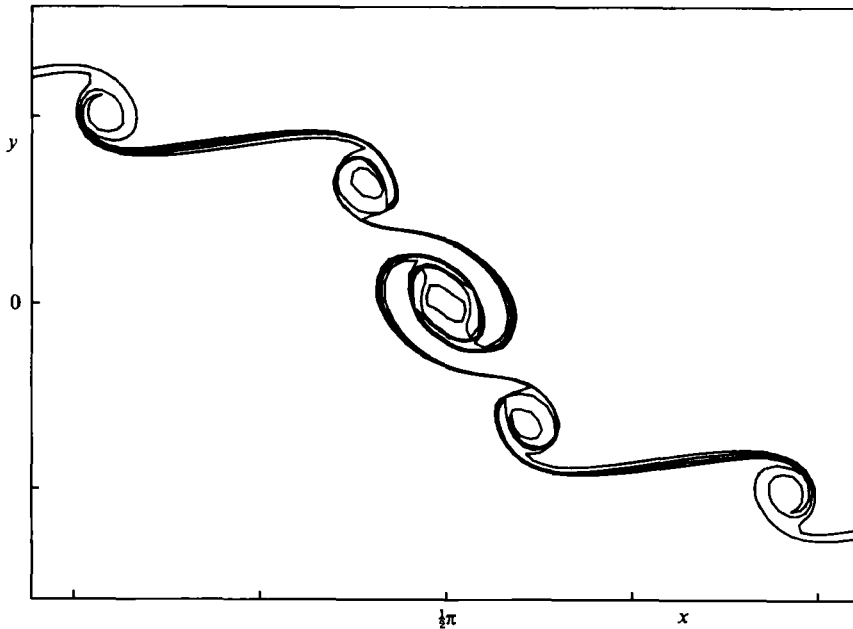FIGURE 15. Magnified view of vortex contours, $a_2 = 25.8$, $\hat{\gamma} = 0.4$, $t = 3$.

FIGURE 16. Magnified view of vortex contours, $a_2 = 25.8$, $\hat{\gamma} = 0.4$, $t = 3.8$.

strain caused by successive pairing events experienced by the primary vortices (Corcos & Sherman 1984), interaction of primary (spanwise) and secondary (stream-wise) vorticity, *strong random variations to perfect spanwise periodicity of secondary vortices which are clearly indicated by experimental observations*, and the possibility of fully three-dimensional instabilities of the vorticity distribution that may destroy
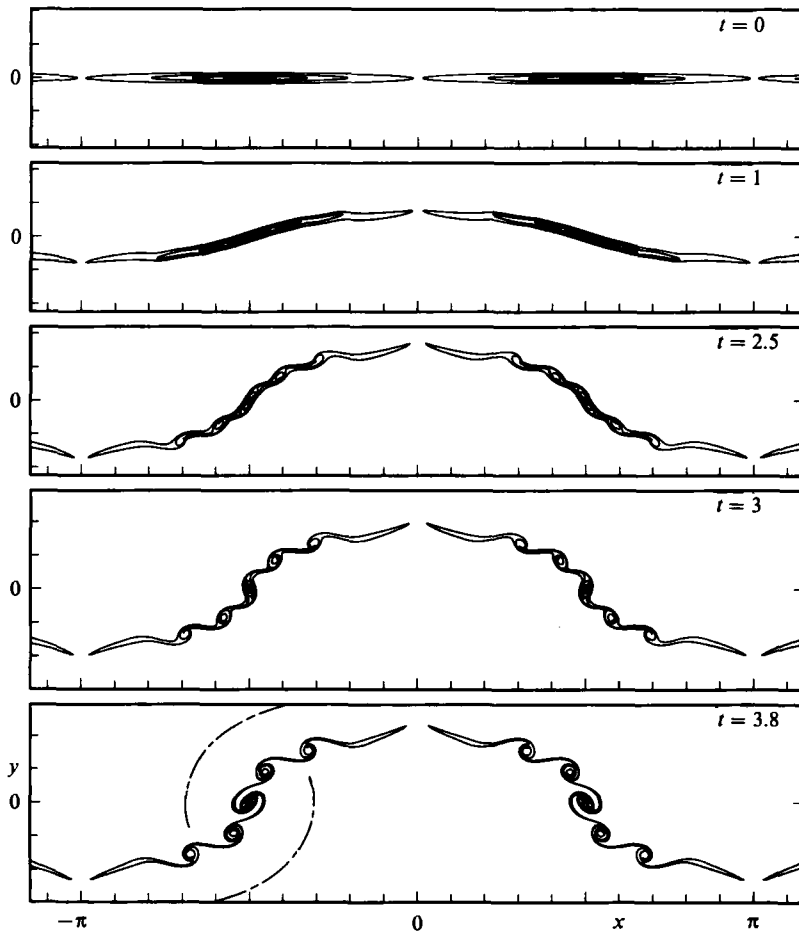
FIGURE 17. Evolution of vortex array, $a_2 = 51.7$, $\hat{\gamma} = 0.1$. Dimensionless times t as shown.

the array coherence on a timescale comparable with that found for the evolution of the vortex fine structure.

The present computations, which we assume to be relevant to the effective infinite-Re_2 limit, and the moderate-Re_2 results of LC are complementary but contain some notable differences. The calculations depicted in figures 4, 7 and 8 of LC at $Re_2 = 508$, 508 and 1950 respectively, and in the present notation, with $a_2 = 8$, $\hat{\gamma} = 0.08$, $a_2 = 11.3$, $\hat{\gamma} = 0.16$ and $a_2 = 18$, $\hat{\gamma} = 0.11$ respectively, are the results most nearly comparable to ours. The beginnings of spiral shear-layer formation can be seen in figure 4 (c–d) and in figure 7, while the onset of local shear instability is evident in the highest-Re_2 case of figure 8. Neither of these trends becomes well developed although it is clear that the suggestion of local instabilities provides the motive for the LC study of nonlinear Burgers-vortex-layer evolution. In the LC simulations the focusing of vorticity by the strain field, and the consequent balance effected by enhanced viscous diffusion appear to efficiently attenuate radial vorticity oscillations characteristic of spiral shear layers, with the result that the spiral vortex tail remains, for example in figure 4 (d), only as an appendage to the well-formed nearly axially symmetric asymptotic, Burgers vortex. By comparison the present results indicate that at effectively infinite Re_2 the nonlinear roll-up of, and the (x, y)-plane longitudinal
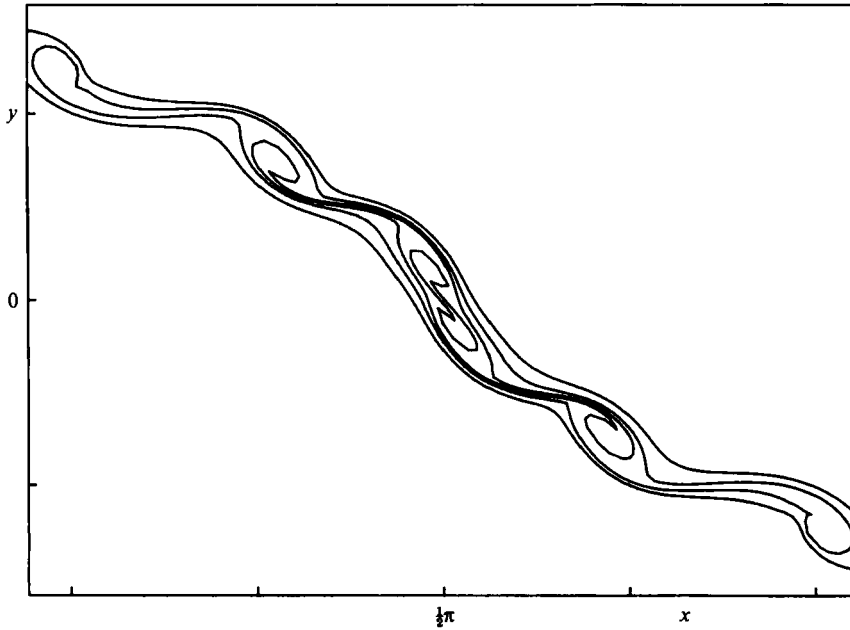
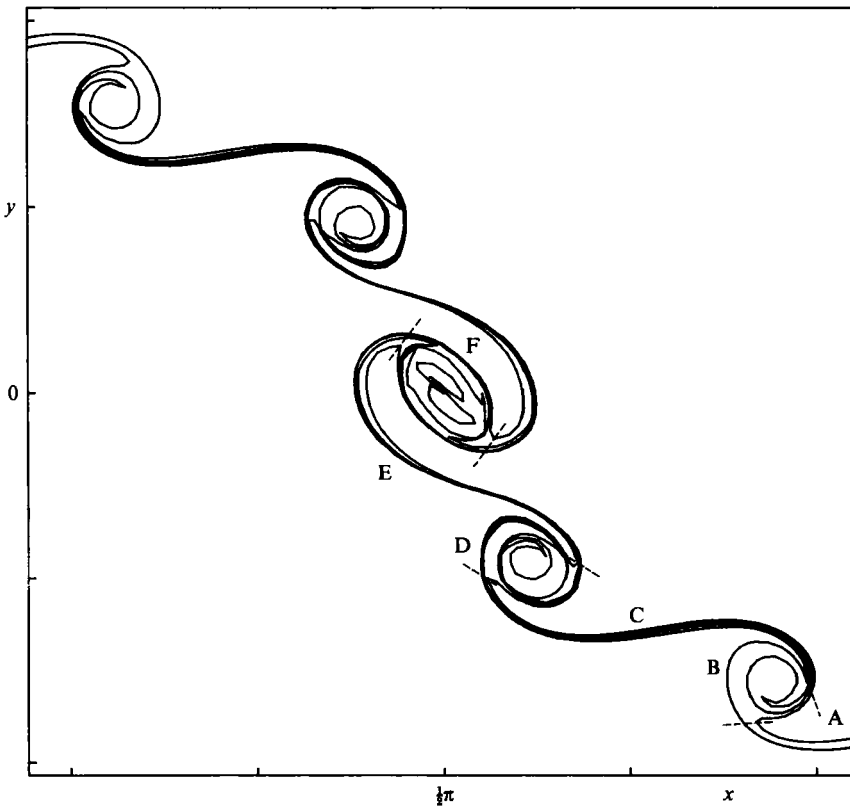FIGURE 18. Magnified view of vortex contours, $a_2 = 51.7$, $\hat{\gamma} = 0.1$, $t = 2.5$.

FIGURE 19. Magnified view of vortex contours, $a_2 = 51.7$, $\hat{\gamma} = 0.1$, $t = 3.8$. Dashed lines indicate division of vortex into a system of cores and connecting braids. Section A extends to the end of the vortex tail.
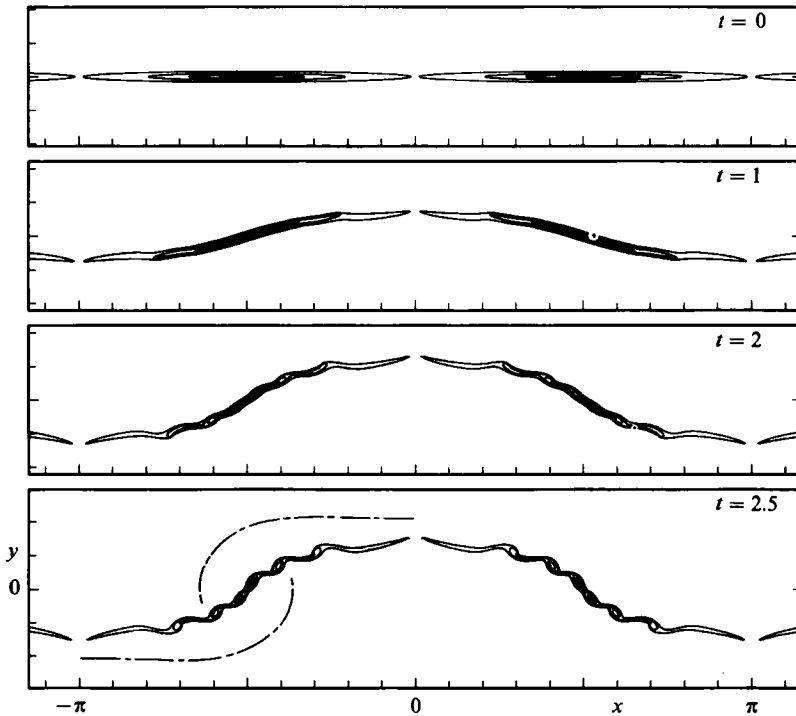
FIGURE 20. Evolution of vortex array, $a_2 = 51.7$, $\hat{\gamma} = 0.2$. Dimensionless times t as shown.
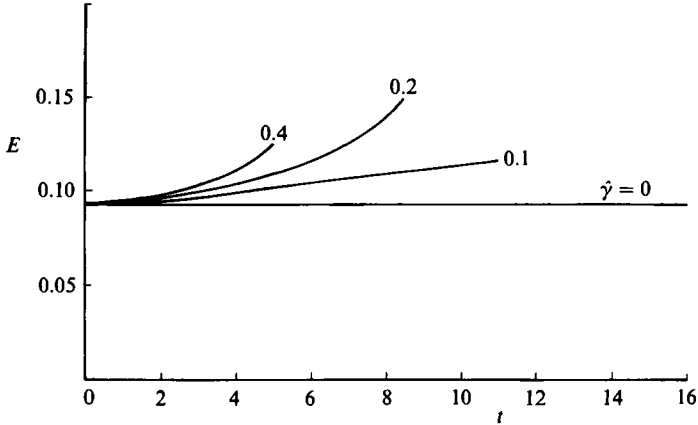

FIGURE 21. Energy of the vortex array per member, $a_2 = 12.7$. Values of $\hat{\gamma}$ as shown.

strain induced on an individual vortex by the rest of the array, can effectively combine to form new spiral vortex layers containing several turns on a timescale comparable with both γ^{-1} and the vorticity focusing timescale. These differences seem to be clearly Reynolds-number dependent, and may be worthy of further study. At large but realistic Re_2, the LC and the present results together suggest a mechanism whereby vortex sheets may be continually created by spiral production following roll-up associated with nonlinear secondary or higher-order instabilities, and destroyed by relaxation via the Lundgren (1982) mechanism towards the equilibrium Burgers vortex. Simultaneously any unrolled vortex layers, such as
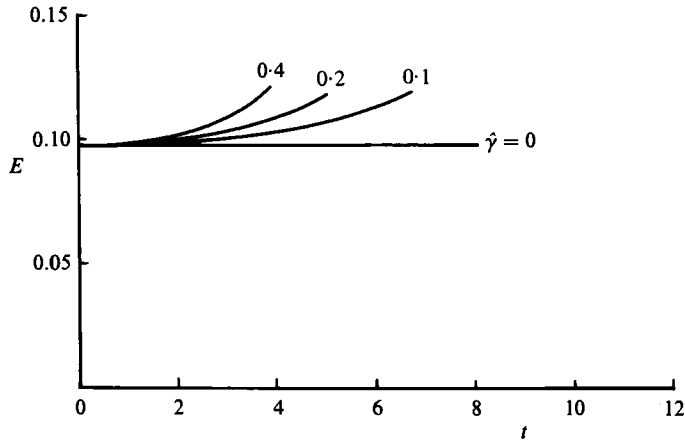
FIGURE 22. Energy of the vortex array per member, $a_2 = 25.7$. Values of $\hat{\gamma}$ as shown.
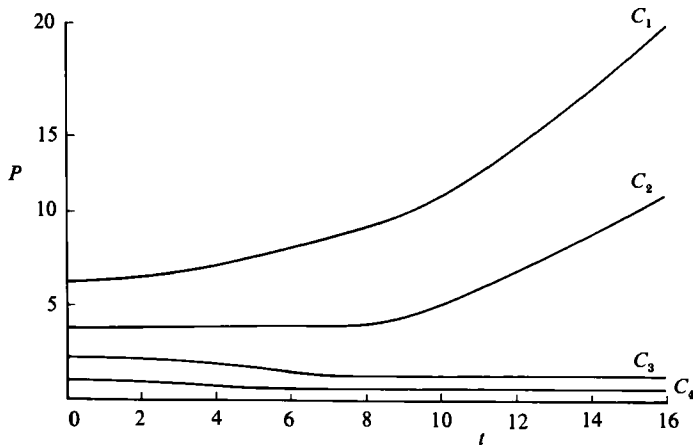
FIGURE 23. Variation of contour perimeter with time t, $a_2 = 12.7$, $\hat{\gamma} = 0$.

trailing vortex filaments might be expected to be stretched towards the local Burgers-vortex-layer thickness δ_2, whereafter disintegration to smaller-scale vortex rods would follow.

Although very highly idealized, the present simulations provide some evidence that the natural vortex dynamics of secondary vortices are capable of producing a spectrum of rod and sheet-like structures of the type observed in flow-visualization studies of mixing-layer streamwise vortices.

Appendix A. Velocity field of the stretching vortex array

Consider first an isolated uniform vortex in the (x, y)-plane whose vortex lines are all initially parallel to the z-axis and are of infinite extent. Let the counterclockwise curve C bound the vortex. Inside C the initial vorticity is $\omega(0)$ and outside C the flow is irrotational. Now let the vortex be subject to a uniform plane-strain field in the
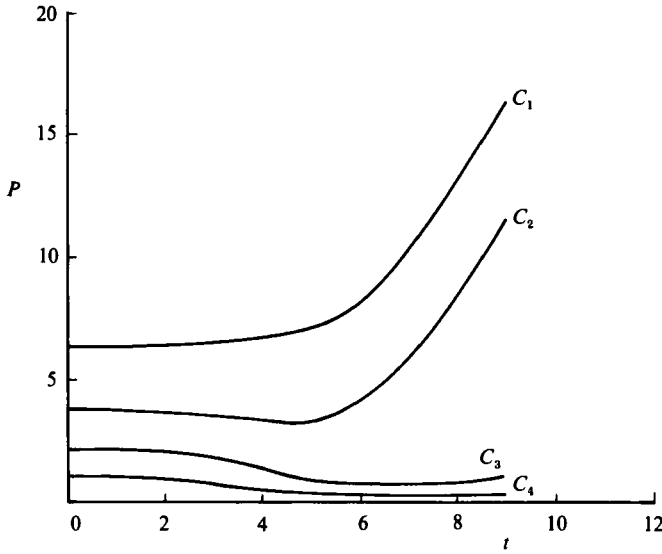
FIGURE 24. Variation of contour perimeter with time t, $a_2 = 25.7$ $\hat{\gamma} = 0.2$.
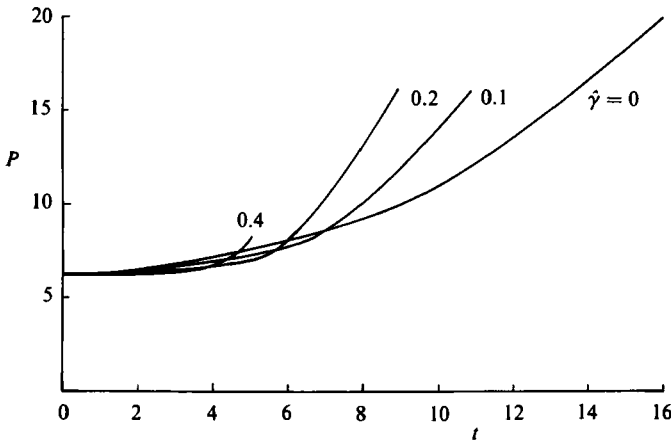

FIGURE 25. Variation of perimeter of outermost contour with times, t, $a_2 = 12.7$. Values of $\hat{\gamma}$ as shown.

(y, z)-plane such that the velocity field can be described by (3.1). Then at time t, the x and y components of velocity at a point (x, y) can be expressed in complex form as (e.g. see equation (10) of Jacobs & Pullin 1985).

$$u_x - \mathrm{i}u_y = \mathrm{i}\gamma y - \frac{\omega(0)\exp{[Q(t)]}}{2\pi\mathrm{i}}\oint_C \frac{y'}{\zeta - \zeta'}\,\mathrm{d}\zeta' - \mu y\omega(0)\exp{[Q(t)]}, \qquad (\mathrm{A}\,1)$$

where $\mu = 1$ if (x, y) is within C and $\mu = 0$ otherwise. In (A 1) the first term on the right-hand side is the stretching-strain contribution to the velocity field and the second and third terms are a decomposition of the vortex-induced velocity into

irrotational and rotational parts respectively. The integral term expresses the irrotational velocity field as a distribution of complex singularities of local density $y \partial \zeta / \partial s$ on C (s is arc length), chosen so as to just cancel the jump in the rotational velocity component as a field point ζ crosses C.

Now consider an infinite array of vortices, each member of which is identical with the isolated vortex described above. Let the centroids of the vortices be $(y_c, x_c + p\lambda)$, $p = -\infty, ..., \infty$. Then summing the contributions of all members of the array to $u_x - iu_y$ gives

$$u_x - iu_y = i\gamma y - \frac{\omega(0)\exp[Q(t)]}{2\lambda i} \oint_C y' \cot\left[\frac{\pi}{\lambda}(\zeta - \zeta')\right] d\zeta' - \mu y \omega(0) \exp[Q(t)]. \quad (A\,2)$$

The integral on the right-hand side of (A 2) may be written as

$$\oint_C (y - y') \cot\left[\frac{\pi}{\lambda}(\zeta - \zeta')\right] d\zeta' - y \oint_C \cot\left[\frac{\pi}{\lambda}(\zeta - \zeta')\right] d\zeta'$$

$$\equiv \oint_C (y - y') \cot\left[\frac{\pi}{\lambda}(\zeta - \zeta')\right] d\zeta' + \mu 2 i\lambda y, \quad (A\,3)$$

where the second integral on the left-hand side of (A 3) has been evaluated using residues. Thus

$$u_x - iu_y = i\gamma y + \frac{\omega(0)\exp[Q(t)]}{2\lambda i} \oint_C (y - y') \cot\left[\frac{\pi}{\lambda}(\zeta - \zeta')\right] d\zeta', \quad (A\,4)$$

and we note that (A 4) is valid for (x, y) inside, outside, or on C. Generalizing (A 4) by inspection to a vortex array whose individual members are defined by a nested contour geometry and vorticity distribution like that described in §3.1, we find

$$u_x - iu_y = i\gamma y + \frac{\exp[Q(t)]}{2\lambda i} \sum_{m=1}^{m} \Delta\omega_m \oint_{C_m} (y - y'_m) \cot\left[\frac{\pi}{\lambda}(\zeta - \zeta'_m)\right] d\zeta'_m, \quad (A\,5)$$

where $\Delta\omega_m = \omega_m(0) - \omega_{m-1}(0)$.

Equation (3.9) follows by first applying (A 5) individually to each member of the typical vortex pair illustrated in figure 2. Secondly, the integrals on the contours of vortex 2 are expressed as integrals on the C_j using the mirror-image symmetry properties of the pair. Finally we let (x, y) be a point on C_j and identify $u_x - iu_y$ in (A 5) with the complex velocity, expressed as $\partial \bar{\zeta}_j / \partial t$, of a material point on C_j with instantaneous coordinate $[x(t), y(t)]$.

Appendix B. Node-insertion/deletion procedure

The node-insertion/deletion scheme was operated to maintain adequate contour resolution while maintaining the required computing resources at manageable levels. The scheme itself is computationally expensive and so was implemented at intervals $\Delta t_2(t)$ where

$$\Delta t_2 = 0.2 \exp(-Q(t)). \quad (B\,1)$$

The node-insertion procedure is a refinement of that used by Jacobs & Pullin (1985). Specifically a node was inserted between $(\zeta_j)_k$ and $(\zeta_j)_{k+1}$ on C_j if

$$|(\zeta_j)_{k+1} - (\zeta_j)_k| > \epsilon^{(3)}, \quad (B\,2a)$$

$$\epsilon^{(3)} = \max[\min(\tfrac{1}{2}d_{\min}, \tfrac{1}{6}\kappa^{-1}, S_{\max}, 4S_{\mathrm{adj}}), 0.021], \quad (B\,2b)$$

$$d_{\min} = \max[S_{\min}, 0.04], \quad (B\,2c)$$

$$S_{\min} = \text{minimum distance of approach of another contour,} \qquad (\text{B } 2d)$$
$$\text{(or non-adjacent part of current contour)}$$

$$\kappa = \text{local contour curvature,} \qquad (\text{B } 2e)$$

$$S_{\max} = \min[0.03 \times (\text{perimeter of } C_j), 0.15], \qquad (\text{B } 2f)$$

$$S_{\text{adj}} = \min[|(\zeta_j)_k - (\zeta_j)_{k-1}|, |(\zeta_j)_{k+2} - (\zeta_j)_{k+1}|]. \qquad (\text{B } 2g)$$

The new node was placed at $e = k + \frac{1}{2}$ by linear interpolation on $[(\zeta_j)_k, (\zeta_j)_{k+1}]$. Cubic interpolation was used for some trials and although it has higher-order accuracy in regions which have a low curvature-to-arc-length ratio, it was much less robust than the linear interpolation in cusp-like segments of the $C_j(t)$ where this ratio was large.

Node deletion operated by deleting node $(\zeta_j)_k$, if $|(\zeta_j)_{k+1} - (\zeta_j)_k| < \epsilon^{(4)} = \max[0.01, \frac{1}{3}\epsilon^{(3)}]$. This simple node deletion was preferred to higher-order interpolation as it reduced the occurrence of slender contour filaments containing negligible circulation and decreased the tendency for contours to fold back upon themselves. The incidence of this type of numerical event remains one of the major problems in the application of the CD technique.

Inadequate description of fine-scale motions is the penalty for minimizing required computing resources. Limits upon the number of nodes inserted are indicated by the empirical constants in (B $2b,c,f$). These constants were chosen so that no single criterion dominated the node distribution, but so that the coherence of the contours and the accuracy of the calculated flow invariants was maintained. Ultimately, the only satisfactory method of testing accuracy is to demonstrate convergence of the CD solution for specific applications, with respect to the constants appearing in (B $2a$–g) that determine the $N_j(t)$. Such convergence was obtained empirically by Jacobs & Pullin (1985) for the vortex-coalescence problem with $M = 1$. Unfortunately a similar demonstration for the present problem proved impractical owing to the very large values of $N_j(t)$ generated quite early in most simulations. We note that general convergence and uniqueness proofs for the CD approximating scheme utilizing node insertion have yet to be established.

REFERENCES

BERNAL, L. P. 1981 The coherent structure of turbulent mixing layers. II. Secondary streamwise vortex structure. Ph.D. thesis, California Institute of Technology.

BREIDENTHAL, R. 1981 Structure in turbulent mixing layers and wakes using a chemical reaction. *J. Fluid Mech.* **109**, 1–24.

BURGERS, J. M. 1948 A mathematical model illustrating the theory of turbulence. *Adv. Appl. Mech.* **1**, 171–196.

CORCOS, G. M. & LIN, S. J. 1984 The mixing layer: deterministic models of a turbulent flow. Part 2. The origin of three-dimensional motion. *J. Fluid Mech.* **139**, 67–95.

CORCOS, G. M. & SHERMAN, F. S. 1984 The mixing layer: deterministic models of a turbulent flow. Part 1. Introduction and two-dimensional flow. *J. Fluid Mech.* **139**, 29–65.

COUËT, B. & LEONARD, A. 1980 Mixing layer simulation by an improved three-dimensional vortex-in-cell algorithm. In *Proc. 7th Intl Conf. on Numerical Methods in Fluid Dynamics*. Stanford, Ames.

JACOBS, P. A. & PULLIN, D. I. 1985 Coalescence of stretching vortices. *Phys. Fluids.* **28**. 1619–1625.

JIMENEZ, J. 1983 A spanwise structure in the plane shear layer. *J. Fluid Mech.* **132**, 319–336.

JIMENEZ, J., COGOLLOS, M. & BERNAL, L. P. 1985 A perspective view of the plane mixing layer. *J. Fluid Mech.* **152**, 125–143.

KADEN, H. 1931 Aufwicklung einer unstabilen Unstetigkeitsflache. *Ing. Arch.* **2**, 140. (English trans. R.A. Lib. Trans. no. 403.)

LAMB, H. 1932 *Hydrodynamics*, 6th edn. Cambridge University Press.

LIN, S. J. & CORCOS, G. M. 1984 The mixing layer: deterministic models of a turbulent flow. Part 3. The effect of plane strain on the dynamics of streamwise vortices. *J. Fluid Mech.* **141**, 139–178.

LUNDGREN, T. S. 1982 Strained spiral vortex model for turbulent fine structure. *Phys. Fluids.* **25**, 2193–2203.

MEIRON, D. I., BAKER, G. R. & ORSZAG, S. A. 1982 Analytic structure of vortex sheet dynamics. Part 1. Kelvin–Helmholtz instability. *J. Fluid Mech.* **114**, 283–298.

MEIRON, D. I., SAFFMAN, P. G. & SCHATZMAN, J. C. 1984 The linear two-dimensional stability of inviscid vortex streets of finite-cored vortices. *J. Fluid Mech.* **147**, 187–212.

MOORE, D. W. & SAFFMAN, P. G. 1973 Axial flow in laminar trailing vortices. *Proc. R. Soc. Lond.* A **333**, 491–508.

NEU, J. 1984a The dynamics of a columnar vortex in an imposed strain. *Phys. Fluids*, **27**, 2397.

NEU, J. 1984b The dynamics of stretched vortices. *J. Fluid Mech.* **143**, 253–276.

OVERMAN, E. A. & ZABUSKY, N. J. 1982 Evolution and merger of isolated vortex structures. *Phys. Fluids*, **25**, 1297–1305.

PIERREHUMBERT, R. T. & WIDNALL, S. E. 1982 The two-and-three dimensional instabilities of a spacially periodic shear layer. *J. Fluid Mech.* **114**, 59–82.

PULLIN, D. I. 1981 The nonlinear behaviour of a constant vorticity layer at a wall. *J. Fluid Mech.* **108**, 401.

PULLIN, D. I. & PHILLIPS, W. R. C. 1981 On a generalization of Kaden's problem. *J. Fluid Mech.* **104**, 45–53.

ROBINSON, A. C. & SAFFMAN, P. G. 1984 Stability and structure of stretched vortices. *Stud. Appl. Maths.* **70**, 163–181.

ROSHKO, A. 1980 The plane mixing layer, flow visualization results and three-dimensional effects. In *The Role of Coherent Structures in Modelling Turbulence and Mixing* (ed. J. Jimenez). Lecture Notes in Physics, vol. 136, pp. 208–217. Springer.

ZABUSKY, N. J., HUGHES, M. H. & ROBERTS, K. V. 1979 Contour Dynamics for the Euler equations in two dimensions. *J. Comp. Phys.* **30**, 96–106.